American Mineralogist, Volume 111, pages 394-409, 2026

Genesis of jordanite-geocronite solid solution series in the Huize Pb-Zn deposit, SW China: Implications for fluid evolution in the late mineralization stage

Songning Meng[1,2,3], Yumiao Meng[1,*], Xiaowen Huang[1,†], Xiangping Gu[4,‡], Zeming Shi[2,3], Ruizhong Hu[1], and Xianwu Bi[1]

[1]State Key Laboratory of Critical Mineral Research and Exploration, Institute of Geochemistry, Chinese Academy of Sciences, Guiyang 550081, China
[2]College of Earth and Planetary Sciences, Chengdu University of Technology, Chengdu 610059, China
[3]Sichuan Province Key Laboratory of Nuclear Techniques in Geosciences, Chengdu 610059, China
[4]College of Geosciences and Info-Physics, Central South University, Changsha 410083, China

Abstract

The Huize Pb-Zn deposit is renowned for its substantial reserves of Pb and Zn, along with significant by-products such as Ge and Ag. As main ore minerals, textures and chemical compositions of sphalerite and galena have been widely studied. However, sulfosalts have received limited attention, and their compositional evolution remains unknown. In this study, a series of Pb-As-Sb sulfosalts is identified in the Huize deposit, which are associated with galena, pyrite, and arsenopyrite in the late mineralization stage. These sulfosalts belong to the jordanite-geocronite solid solution (JGSS) series and include three generations: As-bearing geocronite ($Pb_{14}Sb_{6-x}As_xS_{23}$, $2 \le x \le 4$) (JGSS-1), Sb-rich jordanite ($Pb_{14}As_xSb_{6-x}S_{23}$, $4 \le x \le 5$) (JGSS-2), Sb-bearing jordanite ($Pb_{14}As_xSb_{6-x}S_{23}$, $5 \le x \le 6$) (JGSS-3). Single-crystal X-ray diffraction analysis reveals that the split site (As4/Sb4) can be substituted by As. The occupancies of As1/Sb1 and Pb2/As4/Sb4 sites exhibit higher sensitivity to compositional variations (As, Sb) in the fluids compared to the As2/Sb2 and As3/Sb3 sites. Zoned patterns of Sb-As in JGSS are controlled by various fluid-galena interactions, which play a critical role in the formation of JGSS. Chemical compositions of JGSS reveal that the late-stage ore-forming fluids were predominantly enriched in Sb and As. Geocronite and jordanite likely formed nearly simultaneously through the replacement of galena by Sb-, As-rich fluids under relatively high f_{S_2} and high f_{O_2} conditions. The increasing As/(As+Sb) ratio of JGSS with orebody depth indicates an upward migration of hydrothermal fluids. The presence of As-Sb-bearing minerals in the late stage of hydrothermal Pb-Zn system demonstrates the geochemical anomalies of Sb and As can serve as effective indicators for Pb-Zn mineralization. This study establishes the genetic relationship between JGSS formation and fluid evolution and provides new insights into the geochemical behavior of Sb and As during ore formation.

Keywords: Sulfosalts, geocronite, jordanite, solid solution, Huize Pb-Zn deposit, Southwest China

Introduction

Sulfosalts, also known as thiosalts, comprise a large group of minerals with over 220 valid mineral species, and many additional ones (Moëlo et al. 2008). Pb-As-Sb-S sulfosalts are commonly found in medium- and low-temperature ores of hydrothermal deposits and show a close relationship with sphalerite, galena, and pyrite (e.g., Svanberg 1840; Cook et al. 1998; Bryzgalov et al. 2011; Apopei et al. 2016; Vakh et al. 2019). Jordanite and geocronite are typical minerals in the ternary PbS-As_2S_3-Sb_2S_3 system, which were officially defined as $Pb_{14}(As,Sb)_6S_{23}$ and $Pb_{14}(SbAs)_6S_{23}$, respectively, by the sulfosalt sub-committee of the International Mineralogical Association (IMA) Commission on Ore Mineralogy in 2008 (Moëlo et al. 2008). In nature, these minerals often occur as solid solutions due to mutual substitution between As and Sb sites, typically manifesting as Sb-bearing jordanite and As-bearing geocronite, although pure end-member compositions of As and Sb have been documented (e.g., Jambor 1968; Ito and Nowacki 1974; Birnie and Burnham 1976; Moëlo 1983; Moëlo et al. 2008). Birnie and Burnham (1976) first demonstrated that As substitution for Sb in geocronite is constrained to 4 apfu with As/(As + Sb) ratio of 0.33, because the As6 site cannot incorporate Sb. Biagioni et al. (2016) argued that the increasing Sb content from jordanite to geocronite is accompanied by the progressive substitution of As by Sb at the As6 and Sb4 sites. The current As/Sb site occupancy variations in the jordanite-geocronite solid solution (JGSS) series were constrained to a limited compositional range of $Pb_{14}Sb_{(2.9–3.8)}As_{(2.2–3.1)}S_{23}$ (Biagioni et al. 2016). The complete occupancy variation of the continuous solid solution within the JGSS series, however, remains poorly constrained.

The Sichuan-Yunnan-Guizhou (SYG) Pb-Zn metallogenic province, located on the southwestern margin of the Yangtze Block, is a significant low-temperature metallogenic domain in SW China (e.g., Bao et al. 2017; Yao et al. 2023; Zhang et al. 2024). It hosts over 400 Pb-Zn deposits with an average of

* Corresponding author E-mail: mengyumiao@vip.gyig.ac.cn
† Orcid https://orcid.org/0000-0001-5179-0370
‡ Orcid https://orcid.org/0000-0001-5278-6656

0003-004X/26/0003–394$05.00/DOI: https://doi.org/10.2138/am-2024-9708

200 million tons (Mt) of Pb-Zn ores, making it one of the largest Pb-Zn metallogenic provinces globally (e.g., Liu and Lin 1999; Huang et al. 2003; Hu and Zhou 2012; Meng et al. 2019). Among these, the Huize deposit is a super large Pb-Zn deposit in the SYG metallogenic province, with a Pb and Zn reserve of 7 Mt at Pb + Zn grades of 25% to 35% (e.g., Zhang et al. 2015; Zhao et al. 2023). Moreover, it also hosts economically significant elements such as Ag, Cd, Ge, and Ga (e.g., Bao et al. 2017; Meng et al. 2024; Niu et al. 2024).

The Huize Pb-Zn deposit has been extensively studied in terms of deposit geology (e.g., Han et al. 2007, 2012, 2023), geochemistry (e.g., Zhou et al. 2001; Li et al. 2007a; Meng et al. 2019; Tan et al. 2023), geochronology (e.g., Zhang et al. 2005; Li et al. 2007b; Tang et al. 2019), and the source of ore-forming materials (e.g., Hu et al. 2017; Meng et al. 2019; Oyebamiji et al. 2023). However, systematic investigations into sulfosalts mineralogy in this deposit remain scarce. A few studies reported Sb-bearing sulfosalts, including native Sb, pyrargyrite (Ag_3SbS_3), bournonite ($PbCuSbS_3$), and boulangerite (Pb_5Sb4S_{11}) (Li et al. 2005). These Sb-bearing sulfosalts are mainly distributed above the 1500 m elevation level in the orebody and occur as anhedral grains (<30 μm) included within galena (Li et al. 2005). In this study, JGSS minerals were first identified in the late mineralization stage and are predominantly distributed below the 1500 m elevation level of the orebody. The JGSS minerals include both As-bearing and Sb-bearing sulfosalts such as jordanite and geocronite, providing a good example for studying the genesis of these minerals.

This study carried out a comprehensive investigation of jordanite and geocronite in the Huize Pb-Zn deposit. The main objectives of this study are: (1) to characterize the textural relationships and genetic evolution of different generations of these sulfosalt minerals; (2) to quantitatively analyze variations in site occupancies of As and Sb in the jordanite-geocronite solid solution series through integrated electron probe micro analyzer (EPMA) and single-crystal X-ray diffraction techniques; and (3) to establish a robust genetic model linking the formation of JGSS with late-stage hydrothermal fluid evolution in the Huize Pb-Zn deposit.

Regional Geology

The South China Block comprises the Yangtze Block to the northwest and the Cathaysia Block to the southeast (Fig. 1a). The amalgamation of these blocks formed the Jiangnan

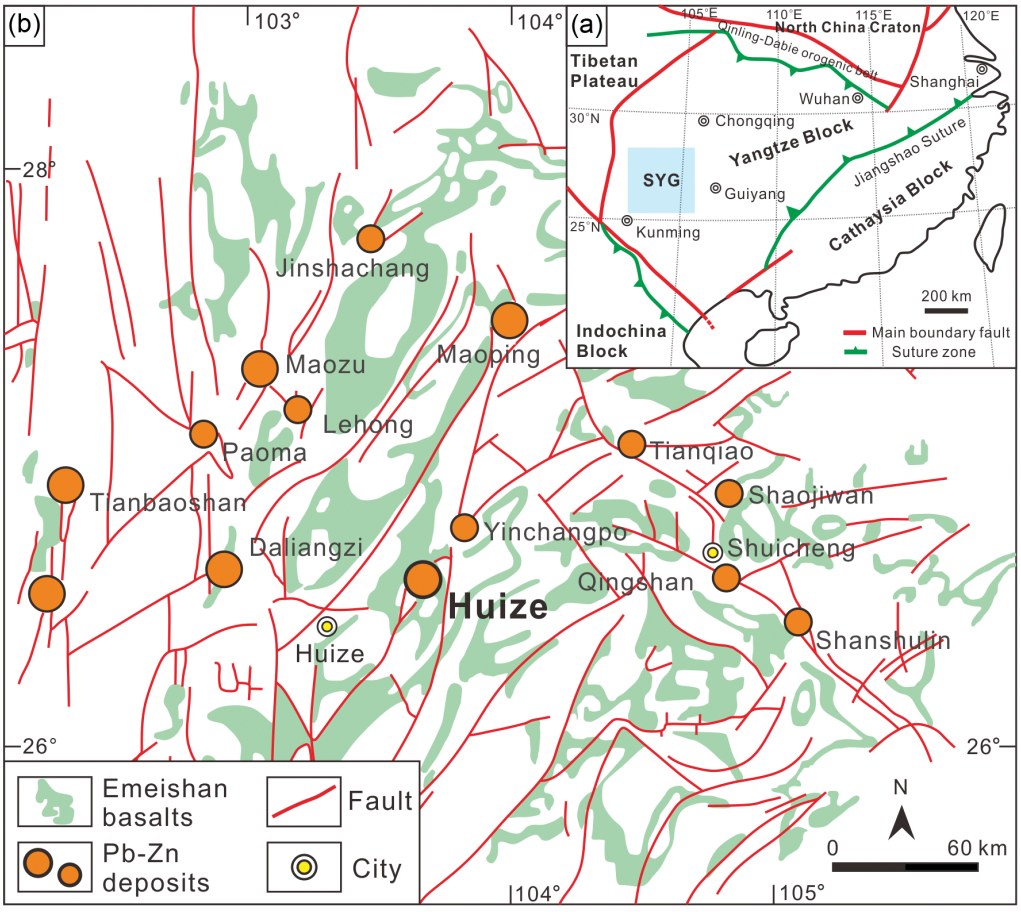

Figure 1. (**a**) Geotectonic location of the Sichuan-Yunnan-Guizhou (SYG) Pb-Zn metallogenic province within the Yangtze Block [modified from Hu et al. (2017)]. (**b**) Simplified geological map showing the distribution of Pb-Zn deposits in the SYG province [modified from Liu and Lin (1999)]. (Color online.)

Orogenic Belt during the Proterozoic, around 820~850 Ma (Li et al. 2009; Wang et al. 2011; Zhao et al. 2011; Wu et al. 2018). The collision with the Indochina Block in the late Permian created the Sanjiang Orogenic Belt (Metcalfe 2013; Wang et al. 2014). The Qinling-Dabie Shan, a late Mesozoic orogenic belt, connects the Yangtze Block with the North China Craton (Fig. 1a) (Mi et al. 2015; Luo et al. 2020). The Yangtze Block consists of Archean-Paleoproterozoic crystalline basement, late Mesoproterozoic to early Neoproterozoic, weakly metamorphosed rocks, and late Neoproterozoic to early Mesozoic marine facies strata (Zhou et al. 2002; Yan et al. 2003).

The SYG Pb-Zn metallogenic province, located on the southwestern margin of the Yangtze Block, is a significant low-temperature metallogenic region and a major source of Pb, Zn, Ag, and Ge in China (Fig. 1a) (e.g., Hu and Zhou 2012; Zhang et al. 2015; Han et al. 2023). This province hosts over 400 Mississippi Valley-type (MVT) Pb-Zn deposits. The exposed strata range from the late Ediacaran to the Quaternary (Li et al. 2020). Key ore-hosting formations include the phosphorous-bearing siliceous dolomite of the Ediacaran Dengying Formation, Devonian dolomite, and Carboniferous Baizuo Formation carbonates (Li et al. 2020; Tan et al. 2023). The distribution of Pb-Zn deposits and carbonates is influenced by well-developed faults and anticlines (Fig. 1b) (Zhou et al. 2013; Zhang et al. 2015). Major regional structures include the NS-trending Anninghe-Lvzhijiang Fault, the NE-trending Mile-Shizhong-Shuicheng Fault, and the NW-trending Kangding-Yiliang-Shuicheng Fault, which collectively form a triangular configuration (Fig. 1b). Additionally, Permian Emeishan basalts are widely distributed in the SYG metallogenic province (Fig. 1b).

Deposit Geology

The Huize Pb-Zn deposit is a super-large deposit located in the central part of the SYG metallogenic province. It is rich in Pb and Zn, and also contains significant amounts of Ag, Ge, Ga, and Cd (e.g., Han et al. 2012; Han et al. 2023). Three mining districts have been mainly discovered, including Kuangshanchang, Qilinchang, and Yinchangpo (Fig. 2) (Han et al. 2007, 2023).

The exposed strata in the Huize Pb-Zn district include rocks from the Ediacaran, Cambrian, Devonian, Carboniferous, and Permian periods (Fig. 2) (Zhou et al. 2001). The most significant ore-hosting rock is the grayish-white, yellowish-red, cream-like, coarse-grained dolostone of the Lower Carboniferous Baizuo Formation (Han et al. 2023). Principal faults, such as the NE-trending Kuangshanchang, Qilinchang, and Yinchangpo Faults, control the spatial distribution of Pb-Zn orebodies (Fig. 2) (Han et al. 2007; Li et al. 2007a). The Huize Pb-Zn deposit has a total reserve exceeding 7 Mt, with an average ore grade of Pb + Zn around 25–35% (Li et al. 2007a; Zhang et al. 2015; Zhao et al. 2023). Major orebodies include No. 1 in Kuangshanchang and No. 3, 6, 8, and 10 in Qilinchang, with ~90% of the reserves located in an interstratified fault zone to parallel the middle and upper Carboniferous Baizuo Formation (Fig. 2) (Han et al. 2007, 2012).

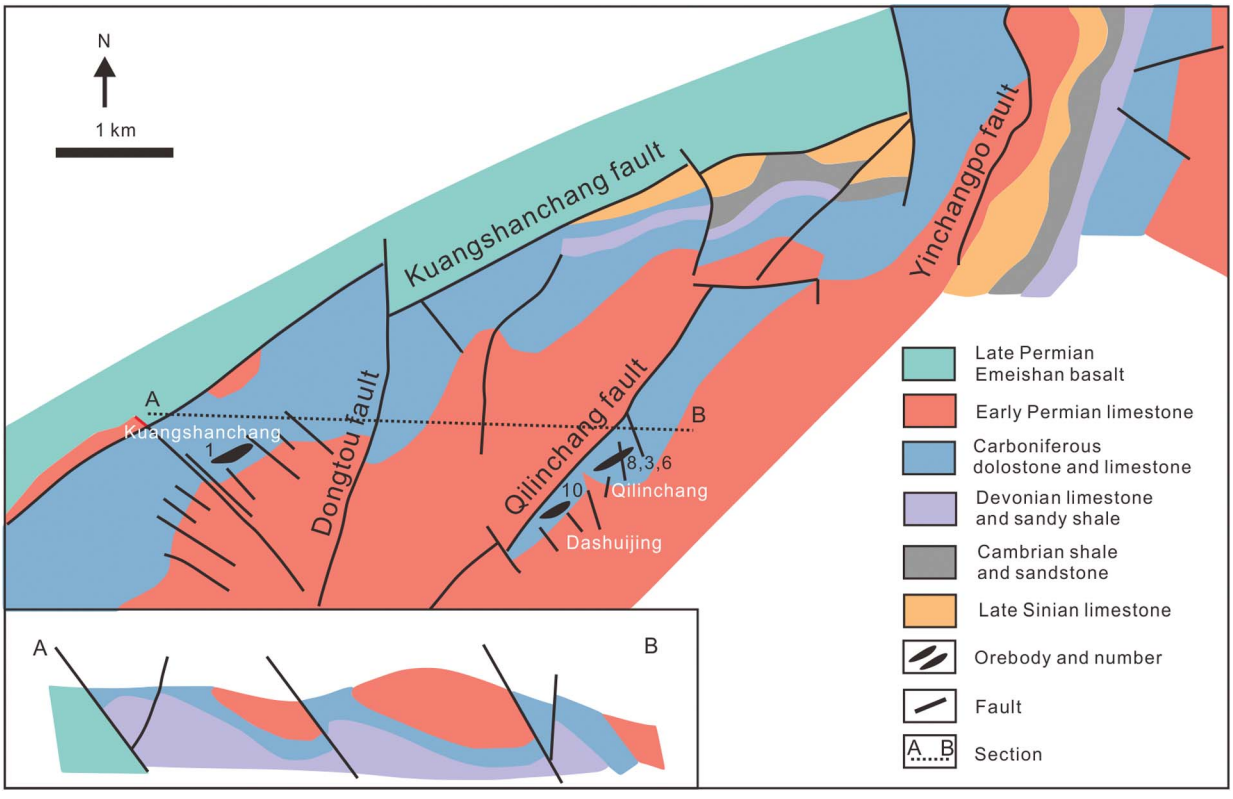

Figure 2. Simplified geological map of the Huize Pb-Zn deposit and cross section [modified from Han et al. (2007)]. (Color online.)

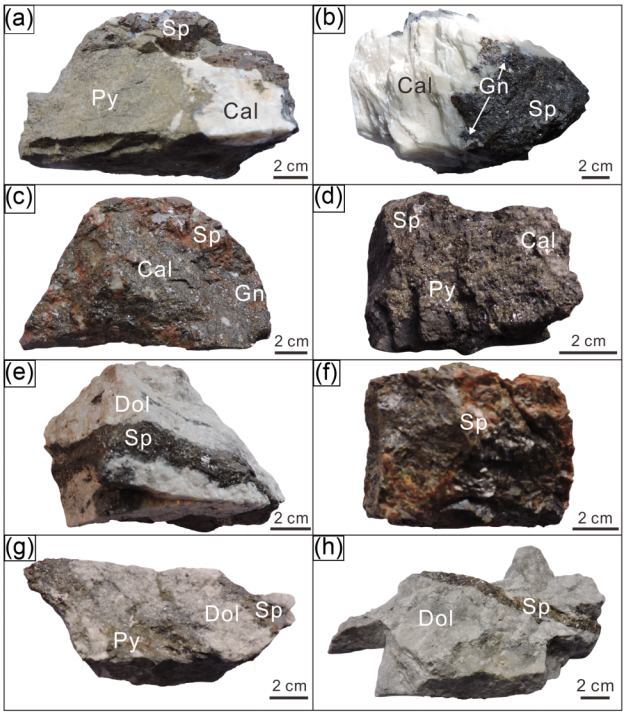

Figure 3. Photos of typical ores from the Huize Pb-Zn deposit. (**a**) Massive ore composed of fine-grained pyrite, light brown, coarse-grained sphalerite, galena, and calcite. (**b**) Massive ore composed of dark brown, coarse-grained sphalerite, galena, and calcite. (**c**) Disseminated ore consisting of fine-grained pyrite, brown coarse-grained sphalerite, and minor galena. (**d**) Disseminated ore comprising coarse-grained pyrite and dark brown, coarse-grained sphalerite. (**e**) Vein ore characterized by dark brown, coarse-grained sphalerite and minor galena. (**f**) Vein ore composed of light brown sphalerite cut by dolomite. Abbreviations: Cal = calcite; Dol = dolomite; Gn = galena; Py = pyrite; Sp = sphalerite. (Color online.)

At the Huize deposit, Zn and Pb ores are highly oxidized in the upper sections, with oxides and sulfides present mainly in the middle sections, and sulfide ores in the deeper parts (Han et al. 2007, 2012). The ores are predominantly massive, disseminated, and vein-like (Fig. 3). The ore minerals primarily include pyrite, sphalerite, and galena, with lesser amounts of arsenopyrite and sulfosalts. Gangue minerals consist of calcite, dolomite, and quartz (Fig. 4). Most minerals exhibit granular textures (Fig. 4). Based on previous studies, the mineralization stages of the deposit can be classified into sedimentary diagenetic, hydrothermal, and supergene stages (Fig. 5) (Han et al. 2000). The hydrothermal stage, which is the primary stage for ore formation, consists of two sub-stages: pyrite-sphalerite and sphalerite-galena. Hydrothermal alteration in the Huize Pb-Zn deposit includes extensive pyritization and dolomitization, accompanied by subordinate calcification, silicification, and clayification (Meng et al. 2019; Tan et al. 2023).

Sampling and Analytical Methods

Sampling

A total of 90 ore samples were collected from the Huize Pb-Zn deposit, with 67 of these samples selected for preparing thin sections. Eight ore examples of sulfosalt-bearing ores were analyzed. Among these samples, sulfosalt-bearing ores were collected from the No. 1 orebody at Kuangshanchang. These samples represent the mineralogical diversity of the orebody across different underground elevations. Detailed sampling information can be found in Online Materials[1] Table S1. Mineral assemblages of ore samples and chemical compositions of minerals were examined using optical microscopy, scanning electron microscopy, and EPMA. Mineral structures were characterized by micro-X-ray diffraction (μ-XRD).

Field Emission Scanning Electron Microscope (FE-SEM)

Petrographic observation was performed using a JEOL JSM-7800F FE-SEM at the State Key Laboratory of Critical Mineral Research and Exploration, Institute of Geochemistry, Chinese Academy of Sciences, Guiyang, China. Thin sections were coated with carbon to enhance the conductivity. Analysis was conducted with an accelerating voltage of 10–15 kV, a beam current of 10 nA, and a beam diameter of 1 μm.

Electron Probe Microanalysis (EPMA)

Major element compositions of sulfosalts were analyzed using a CAMECA SX Five EPMA at the Institute of Geology and Geophysics, Chinese Academy of Sciences, Beijing, China. Operating conditions include an accelerating voltage of 20 kV, a beam current of 30 nA, and a beam size of 2 μm. Counting times were 20 s at the peak and 10 s on either side of the background. Analytical X-rays and calibration standards used were: As (*L*α, InAs); Fe (*K*α, FeS_2); Cu (*K*α, $CuFeS_2$); Zn (*K*α, ZnS); Sb (*L*α, InSb); In (*L*α, InAs); Ag (*L*α, Ag_2Te); Pb (*M*α, PbS); Hg (*L*α, HgS); Ge (*K*α, Ge); and S (*K*α, ZnS). Element mapping of sulfosalts was performed using a JEOL SUPERPROBE JXA-8230 EPMA at the State Key Laboratory of Critical Mineral Research and Exploration, Institute of Geochemistry, Chinese Academy of Sciences, Guiyang, China. Element mapping was conducted using an accelerating voltage of 25 kV, a beam current of 20.05 nA, and a beam size of 0.3 μm.

Single-crystal X-ray Diffraction

Four single crystals ($15 \times 5 \times 4$ μm^3) from the jordanite-geocronite series, including As-bearing geocronite, Sb-rich jordanite, Sb-bearing jordanite, and theoretical jordanite, were prepared using a focused ion beam (FIB) for μ-XRD at the Center for Lunar and Planetary Sciences, Institute of Geochemistry, Chinese Academy of Sciences. Single crystal diffraction studies were conducted with a Rigaku XtaLAB Synergy-DS diffractometer at the State Key Laboratory of Powder Metallurgy, Central South University, Changsha, China. Intensity data were collected using Cu*K*α radiation at 50 kV and 1 mA. X-ray absorption corrections were applied using the multi-scan method, and empirical absorption corrections were performed using CrysAlisPro software, with the SCALE3 ABSPACK scaling algorithm. The crystal structure was solved using SHELXT and refined using the SHELXL program (Sheldrick 2015), packed in the software Olex2 (Dolomanov et al. 2009).

Results

Petrography and Mineralogy

Pb-As-Sb sulfosalts are only present in the late stage of the Huize Pb-Zn deposit. However, these minerals are difficult to identify in hand specimens due to their generally small grain size (<500 μm) and colors similar to galena (Fig. 4). Under reflected light microscopy, these minerals exhibit a blue-gray reflectance and opaque characteristic, darker than galena but lighter than sphalerite (Fig. 6). Their occurrence is typically subhedral to anhedral, often closely associated with galena. Furthermore, SEM imaging revealed that these sulfosalts are homogeneous without zoned texture and a few of these minerals are associated with pyrite and arsenopyrite (Fig. 6).

Three generations of Pb-As-Sb sulfosalts (JGSS-1, -2, and -3) and four generations of pyrite (Py-1, -2, -3, and -4) were systematically distinguished based on their associated mineral assemblages and textural relationships (Figs. 4 and 6). Euhedral

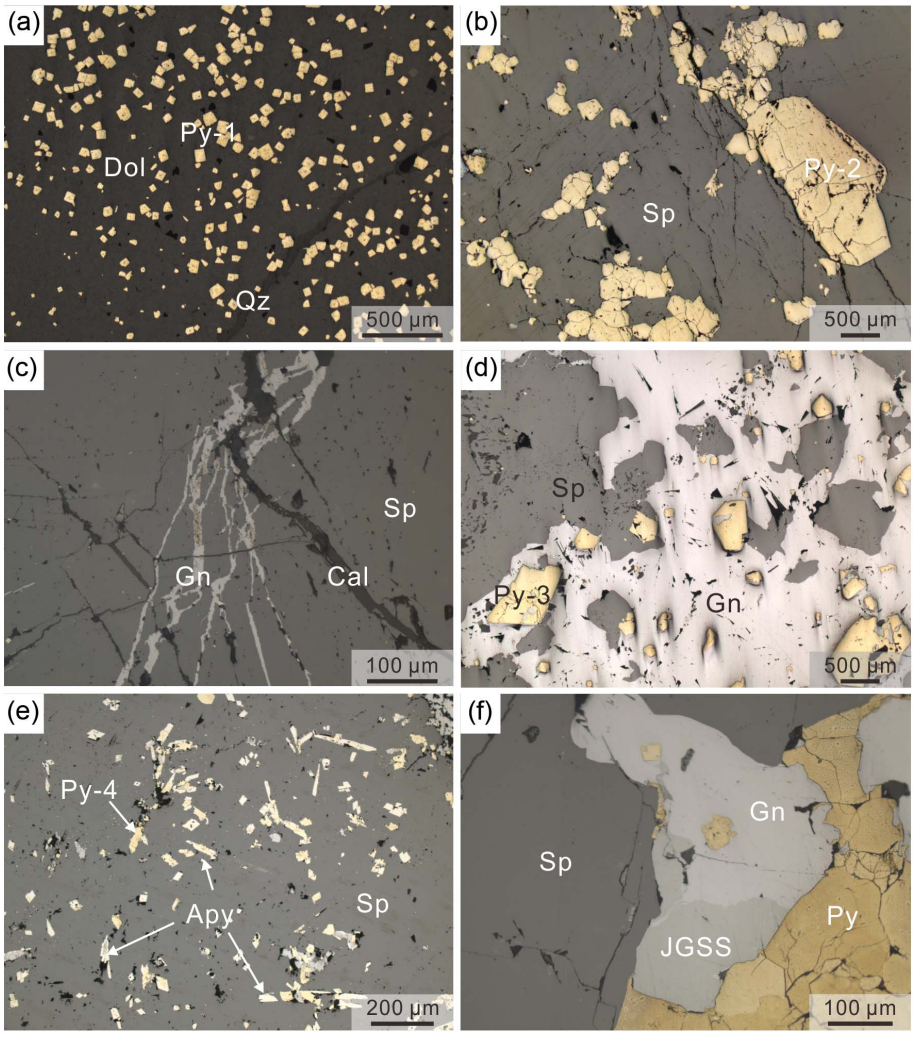

Figure 4. Photomicrographs showing the mineral assemblages and pyrite generations in ores from the Huize Zn-Pb deposit under reflected light. (**a**) Euhedral Py-1 disseminated in dolomite, crosscut by quartz. (**b**) Subhedral pyrite (Py-2) growing in spaces between sphalerite grains. (**c**) Sphalerite crosscut by galena and calcite. (**d**) Subhedral pyrite (Py-3) and sphalerite replaced by galena. (**e**) Fine-grained arsenopyrite and subhedral pyrite (Py-4) disseminated in sphalerite. (**f**) Jordanite-geocronite solid solution series associated with galena. Abbreviations: Apy = arsenopyrite; Cal = calcite; Dol = dolomite; Gn = galena; JGSS = jordanite-geocronite solid solution series; Py = pyrite; Qz = quartz; Sp = sphalerite. (Color online.)

Py-1 (<200 μm) is disseminated in dolomite (Fig. 4a). Subhedral Py-2 (>200 μm) occurs between sphalerite grains (Fig. 4b). Subhedral Py-3 (>200 μm) is encased within galena and subsequently replaced by galena (Fig. 4d). Subhedral Py-4 (<200 μm) coexist with fine-grained arsenopyrite, both replacing sphalerite (Fig. 4e). Subhedral JGSS-1 (<500 μm) is primarily enclosed within galena as discrete inclusions (Figs. 6a–6b), with minor occurrences associated Py-4 and arsenopyrite as inclusions within galena (Fig. 6c). Dissolution voids are observed within these grains (Figs. 6a and 6c). Subhedral JGSS-2 (<500 μm) occurs between sphalerite and galena (Figs. 6d–6e). Anhedral JGSS-3 (>500 μm) intergrows with galena (Fig. 6f). Different generations of JGSS, such as JGSS-1 and -2, can appear in the same galena (Fig. 6g). JGSS-1 grains are commonly small (<100 μm), whereas JGSS-3 can grow larger (>1 cm) (Figs. 6h–6i).

Chemical Compositions of JGSS

EPMA data revealed significant heterogeneity in the chemical composition of jordanite-geocronite solid solution (JGSS), particularly in the As and Sb contents (Table 1; Online Materials[1] Table S1). The chemical formula for the sulfosalts was calculated as $Pb_{(13.12\sim14.23)}As_{(2.28\sim6.25)}Sb_{(0\sim3.77)}S_{23}$, based on S = 23 apfu (Table 1). The JGSS can be divided into three groups based on the As/Sb atomic ratio: As-bearing geocronite (JGSS-1), Sb-rich jordanite (JGSS-1, -2), and Sb-bearing jordanite (JGSS-1, -2, and -3) (Fig. 7a). JGSS-1 has the widest range of As and Sb contents, followed by JGSS-2 and -3. This distinct variation pattern is clearly illustrated in the scatter plot (Fig. 7a), demonstrating a gradual decrease in Sb contents from the early JGSS-1 to the late JGSS-3. Additionally, trace Fe, Zn, Ag, and Ge are present in JGSS (Table 1). JGSS-1 has relatively high Fe contents, with

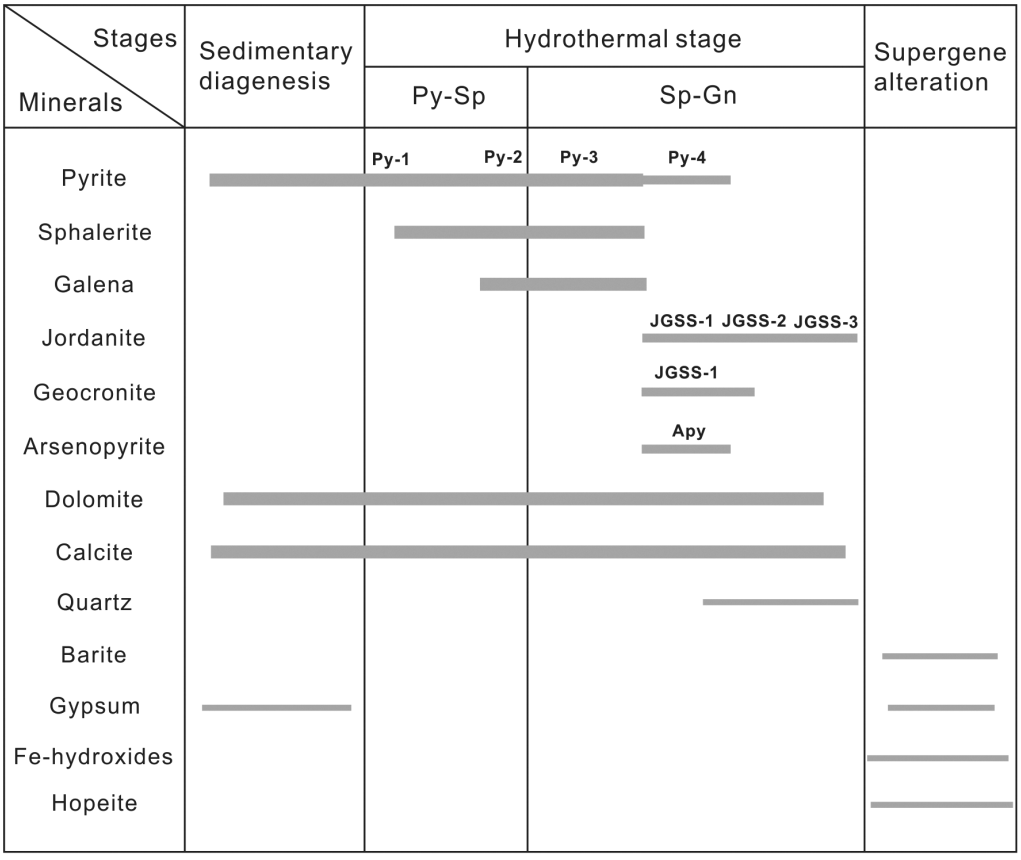

Figure 5. Paragenetic stages of the Huize Pb-Zn deposit showing the generations of the jordanite-geocronite solid solution series [modified from Han et al. (2007)].

a mean of 0.16 wt% (Table 1). Zinc contents are similar between JGSS-1 and -3, with a mean of 0.28 and 0.28 wt%, respectively. However, JGSS-2 has the highest Zn content, with a mean of 0.66 wt% (Table 1). Ag and Ge contents in JGSS-1 are 0.12 and 0.16 wt%, respectively. Cu, In, Hg, and Al contents in JGSS are below the limit of detection (LOD). Furthermore, the As/(As+Sb) ratios in JGSS exhibit a slight vertical zonation within the orebody, showing a gradual decrease from the lower to upper levels (Fig. 7b). The JGSS from the lower levels (1380 m) exhibits significantly higher As/(As+Sb) ratios, with a mean of 0.91 compared to those from the upper levels (1488 m), which have a mean of 0.66. The JGSS collected from the middle-lower levels (1404 m) exhibit a mean As/(As+Sb) ratio of 0.87 (Online Materials[1] Table S1).

EPMA mapping of JGSS-1 and -2 reveals significant heterogeneity in As and Sb contents (Fig. 8). For JGSS-1 enclosed in galena, there is a negative correlation between Sb and As, with Sb and As being more concentrated at the rims and cores of JGSS-1, respectively (Fig. 8a). Additionally, JGSS-1 is richer in S compared to galena, but poorer in Pb compared to galena. For trace elements, JGSS-1 is richer in Ge and Hg compared to sphalerite, but poorer in Cu and Ga compared to galena. There is no obvious difference in Fe, Ag, Zn, Ge, and Hg contents between JGSS-1 and galena (Fig. 8a). JGSS-2, occurring at the interface between galena and sphalerite, also shows a negative correlation between Sb and As. However, in contrast to JGSS-1, Sb is higher in the area adjacent to galena, whereas As is more concentrated in the area distal to galena (Fig. 8b). The variable Fe contents in sphalerite are due to the small pyrite inclusions (Fig. 8b).

Crystallographic Characteristics of the JGSS

The JGSS are isostructural. They share 12 cation sites and 13 anion sites. The only difference is the site occupancy factor (s.o.f.) of As and Sb in As/Sb sites. The unit-cell parameters for these minerals are presented in Tables 2 and 3. The JGSS structure can be described as a stacking of three decahedra, two hendecahedra, two octahedra, and one rectangular pyramid-like unit, with sulfur atoms sharing boundaries (Fig. 9).

The S sites of all the JGSS are similar in the crystal structure (Fig. 9). The site occupation factor (s.o.f.) for S11 is 0.500 in splitting position with a S-S distances 0.71–0.77 Å, while all other S sites have a s.o.f. of 1.000 (Table 4).

The Pb sites in all the JGSS series are similar, with coordination numbers ranging from 5 to 9. Pb1 and Pb9 are coordinated to six sulfur atoms, forming one octahedral geometry with distances ranging from 2.697(17) to 3.335(12) Å (mean = 3.0134 Å). Pb4 to Pb6 are coordinated to seven sulfur atoms, forming a distorted decahedra geometry at distances ranging from 2.662(5) to

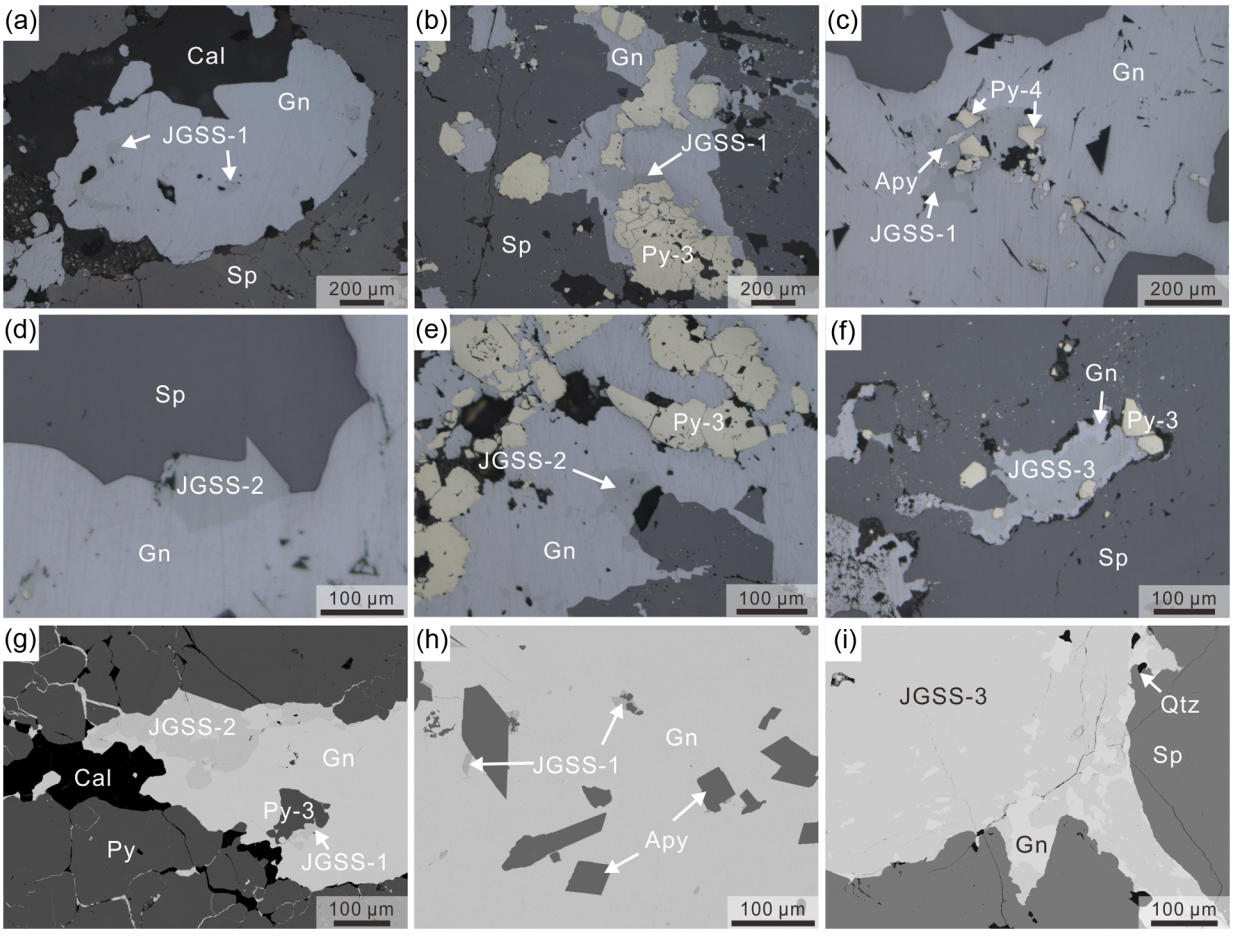

Figure 6. Photomicrographs under reflected light (**a**–**c**) and backscattered electron (BSE) images (**g**–**i**) showing textures of the JGSS from the Huize Pb-Zn deposit. (**a**) Anhedral JGSS-1 presented in galena. (**b**) Subhedral JGSS-1 associated with Py-3 (>200 μm) in galena. (**c**) Subhedral JGSS-1 associated with Py-4 and Apy (<200 μm) in galena. (**d**–**e**) Subhedral JGSS-2 occurring between galena and sphalerite. (**f**) Anhedral JGSS-3 is intergrown with galena. (**g**) Two generations of JGSS (JGSS-1, JGSS-3) associated with galena. (**h**) Fine-grained JGSS-1 (about 10μm) present in galena. (**i**) Coarse-grained JGSS-3 (>500μm) intergrown with galena. Abbreviations as in Figure 4. (Color online.)

3.395(5) Å (mean = 3.0373 Å). Pb3 is coordinated to five sulfur atoms, forming a rectangular pyramid-like geometry with distances ranging from 2.670 to 3.103 Å (mean = 2.9581 Å). Pb7 and Pb8 are coordinated to nine sulfur atoms, forming a hendecahedral geometry with distances ranging from 2.889(11) to 3.286(17) Å (mean = 3.0608 Å). Pb2/As4/Sb4 are coordinated to six sulfur atoms, forming a distorted octahedron with Pb-S distances ranging from 2.631(16) to 3.24 Å (mean = 2.92 Å) (Table 3; Fig. 9).

The Me^{3+} metals, including As^{3+} and Sb^{3+}, are hosted at four positions: As1/Sb1, As2/Sb2, As3/Sb3, and As4/Sb4. As1/Sb1, As2/Sb2, and As3/Sb3 are coordinated to three sulfur atoms, forming a pyramid-like geometry with Me^{3+} atoms at the apex, with distances from 2.170(3) to 2.453(4) Å (mean = 2.2419 Å). It

Table 1. Chemical composition (in wt%) and apfu values for the jordanite-geocronite solid solution series from the Huize Pb-Zn deposit

												apfu			
Mineral			Fe	Zn	Ag	Ge	Pb	As	Sb	S	Total	Pb	As	Sb	S
JGSS-1	n = 116	min	0.10	0.11	0.12	0.16	66.79	4.13	0.03	17.26	98.44	13.12	2.28	0.01	23.00
		max	0.23	0.96	0.12	0.16	71.44	11.75	11.12	18.86	101.90	14.23	6.15	3.77	23.00
		mean	0.16	0.28	0.12	0.16	69.21	8.37	4.60	18.27	100.33	13.49	4.49	1.54	23.00
JGSS-2	n = 23	min	–	0.18	–	–	68.38	8.52	0.01	18.04	98.85	13.26	4.60	0.00	23.00
		max	–	1.59	–	–	71.00	11.71	4.27	18.69	101.54	13.91	6.25	1.43	23.00
		mean	–	0.66	–	–	69.63	10.06	1.97	18.35	100.28	13.51	5.40	0.65	23.00
JGSS-3	n = 5	min	–	0.17	–	–	70.08	11.08	0.02	18.51	100.38	13.35	5.83	0.00	23.00
		max	–	0.45	–	–	71.20	11.53	0.43	18.79	101.46	13.55	6.08	0.14	23.00
		mean	–	0.28	–	–	70.65	11.37	0.25	18.70	101.00	13.44	5.98	0.08	23.00

Notes: Chemical formulas are calculated based on S = 23 apfu. – signifies that measured data are below the minimum limit of detection.

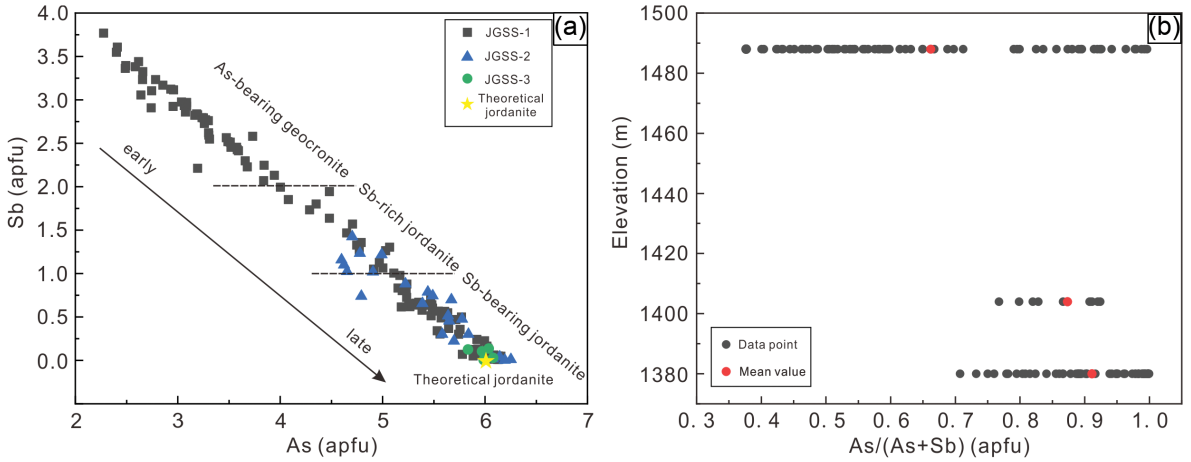

Figure 7. (**a**) Scatter plot showing the As and Sb contents in the JGSS series from the Huize Pb-Zn deposit. (**b**) Scatter plot illustrating the As/(As+Sb) ratios in JGSS samples along the vertical section of the Huize Pb-Zn deposit. (Color online.)

is noted that As3/Sb3 is in a split site about 1.54 Å. The Me^{3+}-S^{2-} distances are generally shorter than Pb^{2+}-S^{2-} distances (Table 3; Fig. 9).

JGSS-1: The Pb2/As4/Sb4 mixed site exhibits a near-equal distribution of Pb (s.o.f. ~0.519) and Sb (s.o.f. ~0.481), with no detectable As occupancy. In contrast, The As1/Sb1 site is strongly dominated by Sb (s.o.f. ~0.942), with only minor As (s.o.f. ~0.058). The As2/Sb2 site is predominantly occupied by As (s.o.f. ~0.854), with Sb showing significantly lower occupancy (s.o.f. ~0.146). The As3/Sb3 is dominated by As, but the s.o.f. of As is only 0.479 due to vacancy defect (Table 4; Fig. 9).

JGSS-2: The Pb2/As4/Sb4 mixed site can accommodate As (s.o.f. ~0.100) compared to JGSS-1 but remain dominated by Pb (s.o.f. ~0.500) and Sb (s.o.f. ~0.400). In contrast to JGSS-1, the As1/Sb site is predominantly occupied by As (s.o.f. ~0.700), with Sb showing significantly lower occupancy (s.o.f. ~0.300). The As2/Sb2 site demonstrates complete As occupation with the s.o.f. of 0.100. Similar to JGSS-1, the As3/Sb3 site only accommodates As with the s.o.f. of 0.500 due to vacancy defect (Table 4; Fig. 9).

JGSS-3: The Pb2/As4/Sb4 mixed site exhibits a near-equal distribution of Pb (s.o.f. ~0.508) and As (s.o.f. ~0.492) compared to JGSS-1. The As1/Sb1 exhibit a complete occupancy of As (s.o.f. ~1.000). The As2/Sb2 and the As3/Sb3 site can accommodate Sb, which remains dominated by As (Table 4; Fig. 9).

Discussion

Atom Variation of the JGSS Unit Cell

The JGSS series is characterized by an isostructural framework in which Pb, As, and Sb occupy distinct crystallographic sites. The structure consists of stacked polyhedral linked by shared S atoms (Fig. 9). The larger ionic radius of Sb^{3+} preferentially occupies the As1/Sb1 site compared to As^{3+}, resulting in the formation of a distorted pyramid structure. This structural configuration is characterized by longer Sb^{3+}-S^{2-} bonds ranging from 2.34 to 2.45 Å, compared to the shorter As^{3+}-S^{2-} bonds of 2.27–2.29 Å (Table 3; Fig. 9) (Shannon 1976). This observation is consistent with experimental studies demonstrating that Sb^{3+} preferentially occupies distorted As1/Sb1 sites under relatively high f_{S_2} conditions (Roland 1968; Biagioni et al. 2016). In contrast, the smaller As^{3+} preferentially occupies the As2/Sb2 and As3/Sb3 sites, where tighter coordination geometries, which are characterized by trigonal pyramids, accommodate shorter As-S bonds (2.13–2.28 Å) (Birnie and Burnham 1976; Biagioni et al. 2016).

In the JGSS structure, Sb predominantly occupies the As1/Sb1 and Pb2/As4/Sb4 sites, whereas As can dominate all four crystallographic sites (Fig. 9). From As-bearing geocronite to theoretical jordanite, site occupancy factors of Sb and As exhibit a systematic trend characterized by a progressive decrease of Sb coupled with a corresponding increase in As at both the Pb2/As4/Sb4 and the As1/Sb1 sites (Figs. 10a–10b). During the evolution of the fluid system, increasing As activity facilitated progressive As substitution at both the As1/Sb1 and As4/Sb4 sites, concomitant with Sb depletion from these sites (Figs. 10a–10b). The Sb-bearing jordanite (JGSS-3) in the later stage exhibits a near complete occupancy of As at As1/Sb1 site, indicating Sb depletion in the fluids at this stage (Fig. 10a). This observed trend is consistent with experimental studies on water-rock reactions demonstrating that As-rich fluid stabilizes As-dominated sulfosalts at relatively low temperatures (Roland 1968; Walia and Chang 1973).

Site occupancy factors for Sb and As at both the As2/Sb2 and As3/Sb3 sites show a similar variation trend, which can be attributed to the occurrence of Sb in As-bearing geocronite and Sb-bearing jordanite (Figs. 10c–10d). The partial vacancy (s.o.f. ~0.5) at the As3/Sb3 site likely results from charge imbalance during As^{3+} substitution for Sb^{3+}, which requires local sulfur deficiency to maintain charge compensation (Table 4) (Krivovichev 2013). In contrast to the As1/Sb1 and As4/Sb4 sites, the As2/Sb2 and As3/Sb3 sites exhibit weaker sensitivity to variations in As and Sb composition in the fluids. This reduced sensitivity can be attributed to the tighter As-S coordination geometry at these sites, which restricts the substitution of larger Sb^{3+} cations (e.g., Shannon 1976; Brown 1981; Krivovichev 2013).

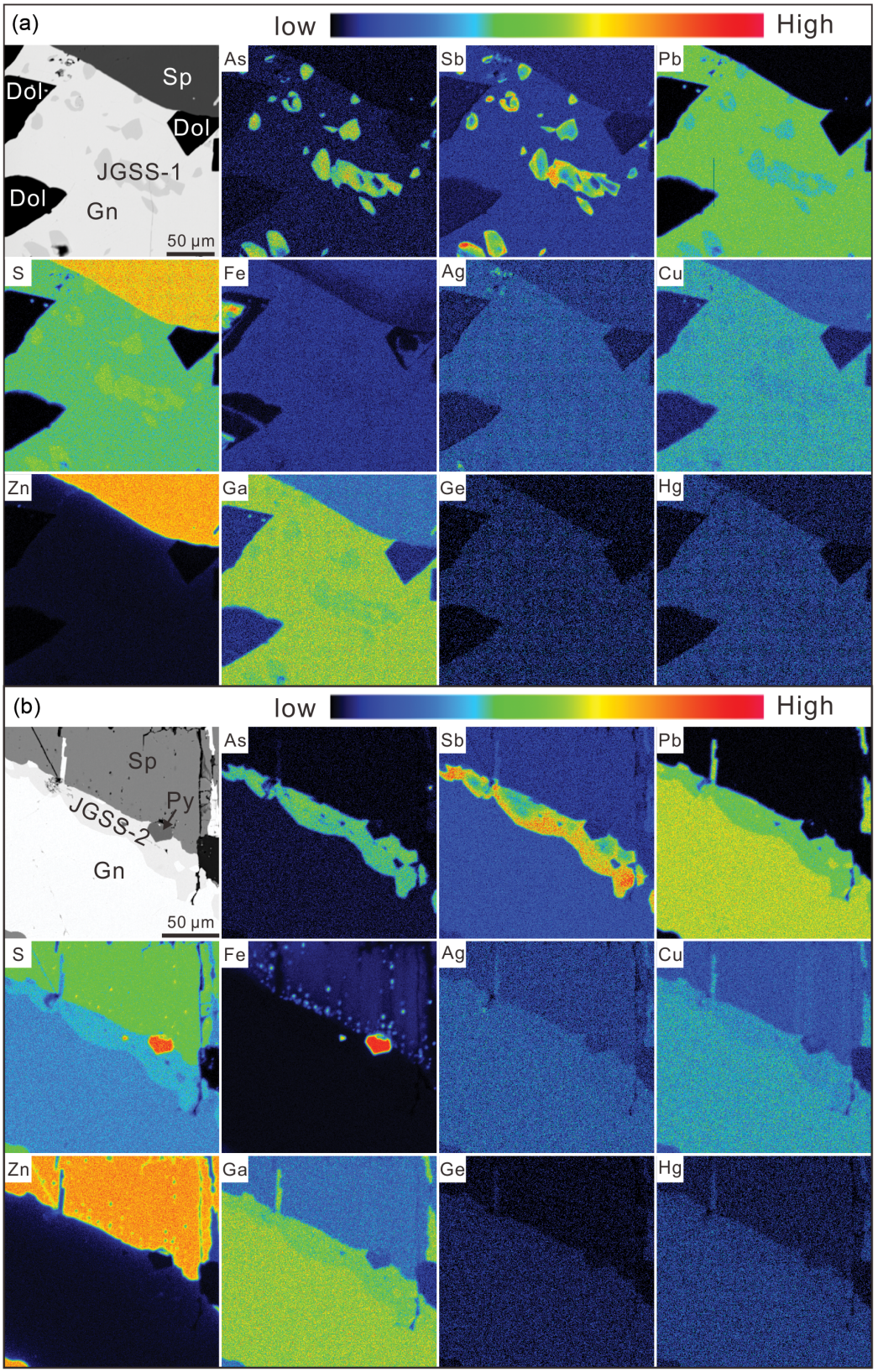

Figure 8. Backscattered electron image and wavelength dispersive X-ray elemental maps of the JGSS series. (**a**) Anhedral JGSS-1 within galena (sample HZ20-74). (**b**) Anhedral JGSS-2 occurring between galena and sphalerite (sample HZ20-18). Abbreviations as in Figure 4. (Color online.)

Table 2. Information on crystal structures and experiment details for the jordanite-geocronite solid solution series

Mineral	JGSS-1	JGSS-2	JGSS-3	Theoretical jordanite
X-ray formula	$Pb_{14}Sb_{3.18}As_{2.79}S_{23}$	$Pb_{14}As_{4.59}Sb_{1.41}S_{23}$	$Pb_{14}As_{5.81}Sb_{0.18}S_{23}$	$Pb_{14}As_6S_{23}$
Crystal system, space group	Monoclinic, $P2_1/m$			
a (Å)	8.9548	8.9309	8.9087	8.9085
b (Å)	31.9410	31.8831	31.8738	37.8781
c (Å)	8.5008	8.4757	8.4633	8.4623
β	118.0170	117.849	117.780	117.769
V (Å^3)	2146.49(84)	2133.89(43)	2126.20(62)	2126.40(91)

Note: The formula was calculated from single-crystal XRD data.

Table 3. Bond distances for metal sites in the jordanite-geocronite solid solution series

Site	<Me-S>	JGSS-1	JGSS-2	JGSS-3	Theoretical jordanite
Pb1 site	<Pb1-S1>	3.016(5) Å	3.005(10) Å	3.000(12) Å	3.001(14) Å
	<Pb1-S2>	2.965(6) Å	2.977(13) Å	3.004(18) Å	3.020(2) Å
	<Pb1-S2>	2.731(5) Å	2.728(10) Å	2.699(14) Å	2.697(17) Å
	<Pb1-S3>	3.301(4) Å	3.324(8) Å	3.335(12) Å	3.334(14) Å
	<Pb1-S5>	2.995(6) Å	2.993(12) Å	2.975(16) Å	2.971(19) Å
	<Pb1-S6>	2.968(4) Å	2.980(8) Å	2.965(10) Å	2.965(12) Å
Pb3 site	<Pb3-S1>	2.997(6) Å	2.930(9) Å	2.915(11) Å	2.917(13) Å
	<Pb3-S2>	3.013(13) Å	2.987(13) Å	2.963(18) Å	2.950(3) Å
	<Pb3-S3>	2.997(6) Å	3.014(11) Å	3.045(15) Å	3.040(19) Å
	<Pb3-S4>	3.032(4) Å	3.086(9) Å	3.103(12) Å	3.098(14) Å
	<Pb3-S5>	2.670(5) Å	2.674(10) Å	2.687(13) Å	2.686(14) Å
Pb4 site	<Pb4-S3>	3.091(5) Å	3.065(11) Å	3.042(15) Å	3.047(19) Å
	<Pb4-S4>	3.066(4) Å	3.037(9) Å	3.035(11) Å	3.038(12) Å
	<Pb4-S5>	3.395(5) Å	3.388(9) Å	3.361(12) Å	3.359(14) Å
	<Pb4-S7>	3.025(5) Å	3.033(10) Å	3.030(14) Å	3.029(17) Å
	<Pb4-S8>	2.982(6) Å	2.968(12) Å	2.956(16) Å	2.960(2) Å
	<Pb4-S10>	2.662(5) Å	2.681(9) Å	2.692(11) Å	2.697(14) Å
	<Pb4-S11>	3.150(7) Å	3.166(16) Å	3.200(2) Å	3.210(3) Å
Pb5 site	<Pb5-S3>	2.918(5) Å	2.908(10) Å	2.906(14) Å	2.910(16) Å
	<Pb5-S5>	2.952(6) Å	2.941(12) Å	2.942(16) Å	2.944(18) Å
	<Pb5-S6>	3.031(4) Å	3.014(8) Å	3.020(11) Å	3.022(14) Å
	<Pb5-S8>	3.239(4) Å	3.229(9) Å	3.209(12) Å	3.198(14) Å
	<Pb5-S9>	2.967(4) Å	2.976(8) Å	2.960(10) Å	2.963(12) Å
	<Pb5-S10>	2.976(6) Å	2.975(12) Å	2.978(15) Å	2.979(19) Å
	<Pb5-S12>	3.1935(13) Å	3.196(3) Å	3.205(4) Å	3.206(2) Å
Pb6 site	<Pb6-S4>	2.942(4) Å	2.934(9) Å	2.930(12) Å	2.933(13) Å
	<Pb6-S5>	2.884(5) Å	2.884(10) Å	2.873(12) Å	2.876(14) Å
	<Pb6-S6>	3.016(5) Å	2.995(10) Å	2.994(14) Å	2.995(17) Å
	<Pb6-S7>	3.209(5) Å	3.201(10) Å	3.188(15) Å	3.199(18) Å
	<Pb6-S9>	2.974(6) Å	2.969(11) Å	2.946(15) Å	2.953(18) Å
	<Pb6-S10>	2.997(5) Å	3.008(9) Å	3.015(10) Å	3.008(13) Å
	<Pb6-S13>	3.2078(10) Å	3.214(3) Å	3.222(3) Å	3.222(4) Å
Pb7 site	<Pb7-S7>	3.262(5) Å	3.281(9) Å	3.297(15) Å	3.286(17) Å
	<Pb7-S9>	3.198(5) Å	3.210(11) Å	3.238(13) Å	3.229(16) Å
	<Pb7-S10>	2.924(5) Å	2.902(9) Å	2.889(11) Å	2.894(14) Å
	<Pb7-S11>	2.900(11) Å	2.900(2) Å	2.900(3) Å	2.910(4) Å
	<Pb7-S12>	2.959(7) Å	2.943(13) Å	2.934(18) Å	2.948(18) Å
Pb8 site	<Pb8-S8>	3.222(5) Å	3.241(10) Å	3.269(14) Å	3.283(17) Å
	<Pb8-S9>	3.223(5) Å	3.235(10) Å	3.258(11) Å	3.255(14) Å
	<Pb8-S10>	2.931(6) Å	2.910(11) Å	2.898(14) Å	2.895(18) Å
	<Pb8-S11>	2.890(8) Å	2.908(14) Å	2.885(15) Å	2.890(2) Å
	<Pb8-S13>	2.961(6) Å	2.949(12) Å	2.939(15) Å	2.930(16) Å
Pb9 site	<Pb9-S7>	3.070(15) Å	3.070(10) Å	3.083(15) Å	3.081(18) Å
	<Pb9-S8>	3.082(6) Å	3.096(11) Å	3.106(15) Å	3.104(19) Å
	<Pb9-S12>	2.934(6) Å	2.949(13) Å	2.949(15) Å	2.930(3) Å
	<Pb9-S13>	2.901(9) Å	2.883(18) Å	2.880(3) Å	2.890(3) Å
Pb2/As4/Sb4 site	<Pb2/As4/Sb4-S1>	<Sb4-S1> 2.678(5) Å	<As4-S1> 2.681(9) Å	<As4-S1> 2.666(13) Å	<As4-S1> 2.666(13) Å
	<Pb2/As4/Sb4-S1>	<Sb4-S1> 2.753(6) Å	<As4-S1> 2.745(12) Å	<As4-S1> 2.720(16) Å	<As4-S1> 2.715(18) Å
	<Pb2/As4/Sb4-S2>	<Sb4-S2> 2.683(5) Å	<As4-S2> 2.661(10) Å	<As4-S2> 2.633(15) Å	<As4-S2> 2.631(16) Å
As1/Sb1 site	<As1/Sb1-S3>	<Sb1-S3> 2.453(4) Å	<Sb1-S3> 2.367(9) Å	<As1-S3> 2.286(12) Å	<As1-S3> 2.284(16) Å
	<As1/Sb1-S4>	<Sb1-S4> 2.412(6) Å	<Sb1-S4> 2.360(12) Å	<As1-S4> 2.273(16) Å	<As1-S4> 2.275(19) Å
	<As1/Sb1-S6>	<Sb1-S6> 2.440(5) Å	<Sb1-S6> 2.344(9) Å	<As1-S6> 2.271(13) Å	<As1-S6> 2.267(15) Å
As2/Sb2 site	<As2/Sb2-S7>	<As2-S7> 2.270(6) Å	<As2-S7> 2.243(13) Å	<As2-S7> 2.241(19) Å	<As2-S7> 2.240(3) Å
	<As2/Sb2-S8>	<As2-S8> 2.267(5) Å	<As2-S8> 2.234(10) Å	<As2-S8> 2.129(13) Å	<As2-S8> 2.229(16) Å
	<As2/Sb2-S9>	<As2-S9> 2.276(5) Å	<As2-S9> 2.246(9) Å	<As2-S9> 2.229(13) Å	<As2-S9> 2.246(15) Å
As3/Sb3 site	<As3/Sb3-S11>	<As3-S11> 2.222(18) Å	<As3-S11> 2.196(16) Å	<As3-S11> 2.180(3) Å	<As3-S11> 2.170(3) Å
	<As3/Sb3-S12>	<As3-S12> 2.222(9) Å	<As3-S12> 2.222(19) Å	<As3-S12> 2.220(3) Å	<As3-S12> 2.220(3) Å
	<As3/Sb3-S13>	<As3-S13> 2.221(9) Å	<As3-S13> 2.222(14) Å	<As3-S13> 2.219(17) Å	<As3-S13> 2.220(3) Å

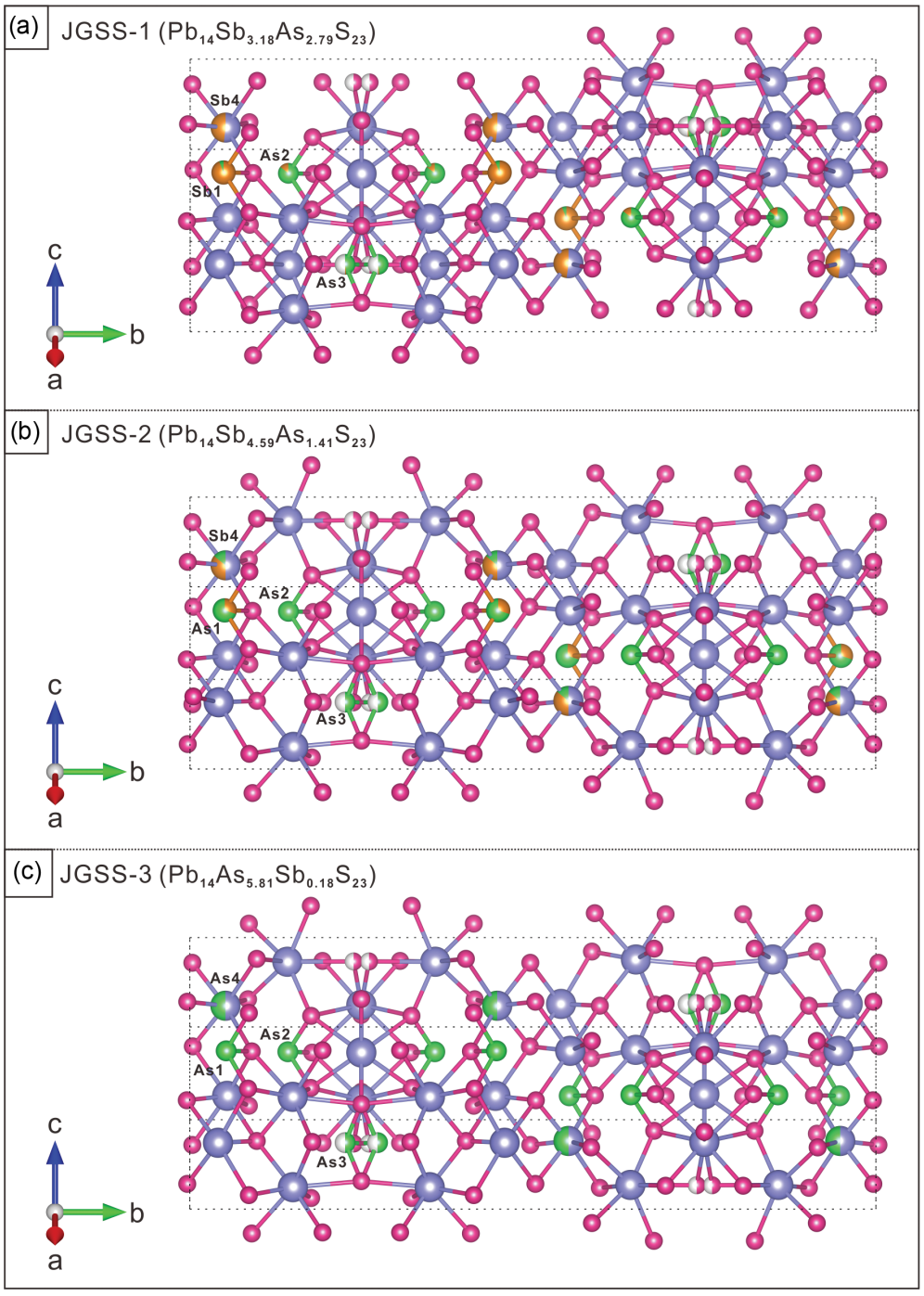

Figure 9. Crystal structures of the jordanite-geocronite solid solution series. (**a**) As-bearing geocronite (HZ20-28-1). (**b**) Sb-rich jordanite (HZ20-54). (**c**) Sb-bearing jordanite (HZ20-18). Balls: blue = Pb sites; orange = Sb sites; green = As sites; red = S sites. (Color online.)

Formation of the JGSS

The crystallographic characteristics and chemical composition of the JGSS are crucial for understanding the formation of JGSS in the late stage of the Huize Pb-Zn deposit. Studies on the genesis of JGSS formed under natural conditions are limited, most focusing on experiments from water-rock reactions (e.g., Roland 1968; Walia and Chang 1973).

Sulfosalts in the Pb-As-Sb-S system can be formed by hydrothermal, sedimentary, and metamorphic processes (e.g., Qiu 2000; Shu et al. 2018; Liu et al. 2023; Sun et al. 2023). The Huize Pb-Zn deposit was formed by hydrothermal processes based on previous studies (e.g., Han et al. 2023; Cui et al. 2024; Zhang et al. 2024). The hydrothermal stage of this deposit is divided into pyrite-sphalerite and sphalerite-galena sub-stages

Table 4. Site occupation factors (s.o.f.) for meta sites in the jordanite-geocronite solid solution series

Site	JGSS-1	JGSS-2	JGSS-3	Theoretical jordanite
Pb1	1.000	1.000	1.000	1.000
Pb2/As4/Sb4	(Pb2/Sb4) 0.519/0.481	(Pb2/As4/Sb4) 0.500/0.100/0.400	(Pb2/As4) 0.508/0.492	(Pb2/As4) 0.5
Pb3	1.000	1.000	1.000	1.000
Pb4	1.000	1.000	1.000	1.000
Pb5	1.000	1.000	1.000	1.000
Pb6	1.000	1.000	1.000	1.000
Pb7	1.000	1.000	1.000	1.000
Pb8	1.000	1.000	1.000	1.000
Pb9	1.000	1.000	1.000	1.000
As1/Sb1	(As1/Sb1) 0.058/0.942	(As1/Sb1) 0.700/0.300	(As1) 1.000	(As1) 1.000
As2/Sb2	(As2/Sb2) 0.854/0.146	(As2) 1.000	(As2/Sb2) 0.940/0.060	(As2) 1.000
As3/Sb3	(As3/Sb3) 0.479/0.021	(As3) 0.5	(As3/Sb3) 0.470/0.030	(As3) 0.5
S1	1.000	1.000	1.000	1.000
S2	1.000	1.000	1.000	1.000
S3	1.000	1.000	1.000	1.000
S4	1.000	1.000	1.000	1.000
S5	1.000	1.000	1.000	1.000
S6	1.000	1.000	1.000	1.000
S7	1.000	1.000	1.000	1.000
S8	1.000	1.000	1.000	1.000
S9	1.000	1.000	1.000	1.000
S10	1.000	1.000	1.000	1.000
S11	0.500	0.500	0.500	0.500
S12	1.000	1.000	1.000	1.000
S13	1.000	1.000	1.000	1.000

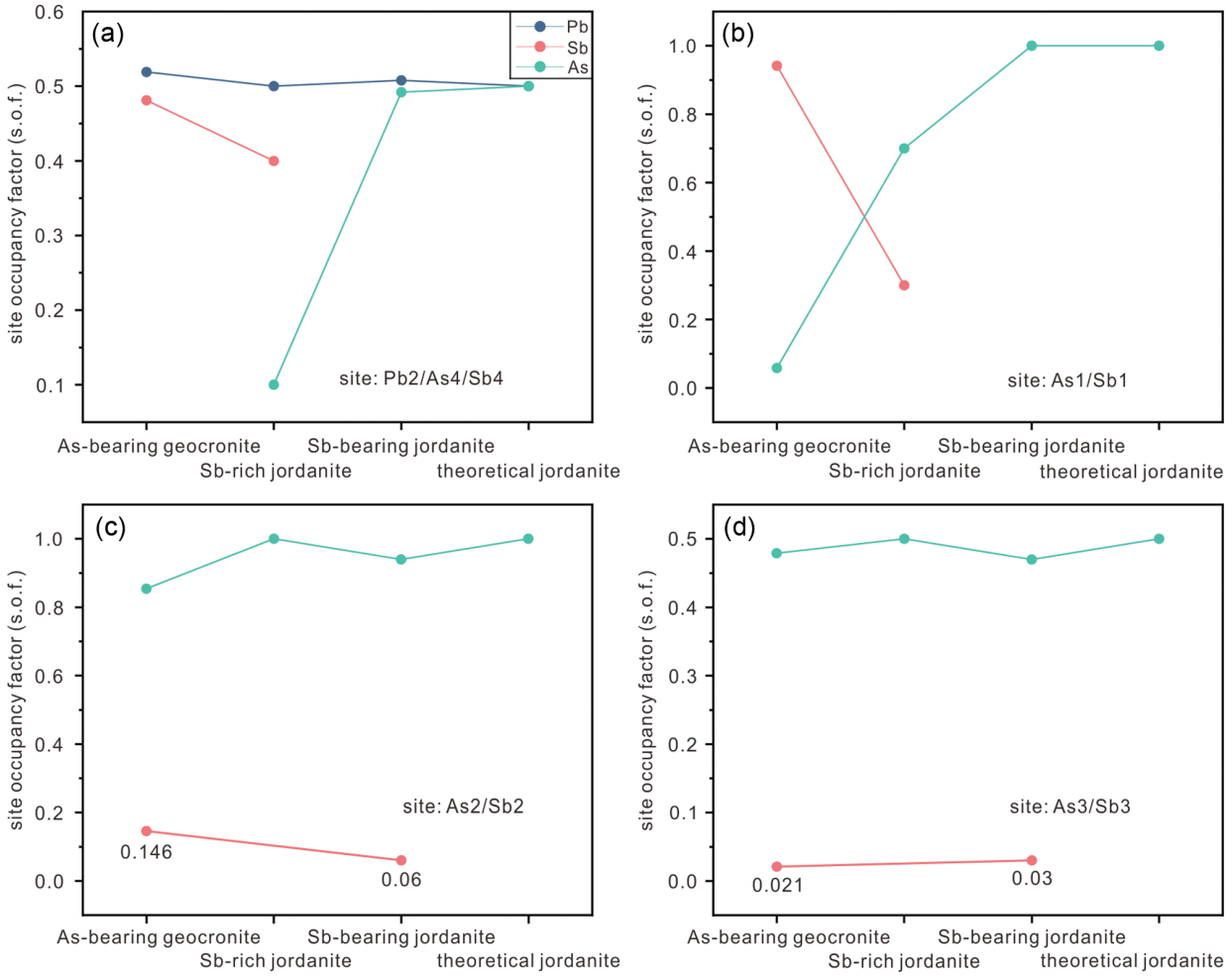

Figure 10. Site occupancy factor of atoms (Pb, Sb, and As) in the jordanite-geocronite solid solution series from the Huize Pb-Zn deposit: (**a**) Pb2, As4, and Sb4 site; (**b**) As1 and Sb1 site; (**c**) As2 and Sb2 site; (**d**) As3 and Sb3 site. (Color online.)

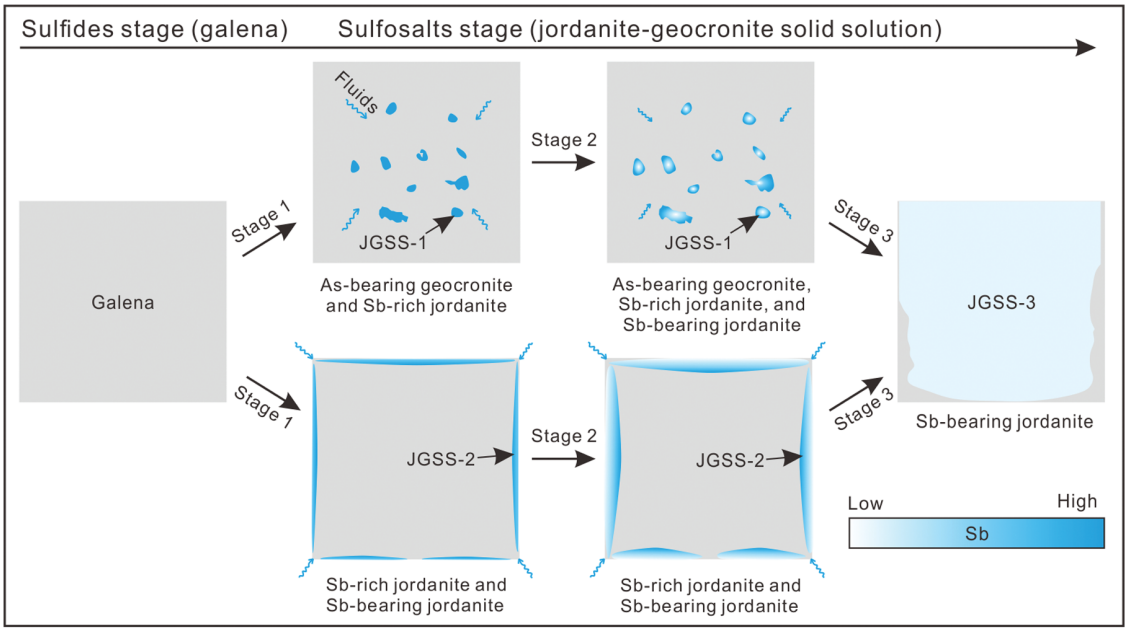

Figure 11. A schematic model illustrating paragenic evolution of the JGSS series in the Huize Pb-Zn deposit. Abbreviations as in Figure 4. (Color online.)

(Fig. 5). The JGSS is texturally related to galena. They are enclosed by galena (e.g., JGSS-1), grow along the margins of galena (e.g., JGSS-2), and are intergrown with galena (e.g., JGSS-3) (Fig. 6). This textural relationship suggests that JGSS primarily forms during the late-stage mineralization, similar to deposits such as the Berezitovoe in Russia, the Pollone in Italy, and the Liziping and Fulongchang in China (e.g., Biagioni et al. 2016; Vakh et al. 2016, 2019; Liu et al. 2023).

Sulfosalts can form by three main mechanisms, including co-precipitation with other sulfides, solid solution exsolution, and mineral-fluid interaction (Cook et al. 1998; Slater et al. 2019; Dincă et al. 2025). Exsolution from solid solutions requires the precursor mineral to be enriched in As and Sb (Slater et al. 2019). Arsenic exhibits limited solubility in galena; hence, it is difficult to form extensive As-rich sulfosalts through exsolution from galena (Renock and Becker 2011). Furthermore, oriented solid solution textures similar to those in galena from the Ivigtut deposit in Greenland were absent (Karup-Moeller 1971). Given that a significant amount of sulfur had already precipitated as sulfides, the late-stage fluids were likely sulfur-depleted. Therefore, co-precipitation with sulfides and solid solution exsolution may not have been the primary mechanism responsible for the extensive formation of JGSS in the Huize deposit.

Petrographic observations demonstrate that the late-stage mineral assemblages (Py-4, arsenopyrite, and JGSS) exhibit replacement textures with visible voids within galena and sphalerite (Figs. 4e and 6a). Replacement reactions between hydrothermal fluids and sulfides can lead to the sulfidation of As^{3-} in As-bearing pyrite and arsenopyrite to As^{3+} in JGSS under a relatively high f_{S_2} (Biagioni et al. 2016). Therefore, the formation of JGSS is likely attributed to a dissolution-reprecipitation process during the replacement of galena by hydrothermal fluids. During fluid-galena interaction, Sb in hydrothermal fluids preferentially reacts with galena at reaction fronts under relatively high f_{O_2} conditions, resulting in Sb-enriched JGSS along the rim of galena (Figs. 8a–8b) (Tolstykh et al. 2025). Galena provides the necessary Pb and S for the formation of JGSS, accounting for the precipitation of abundant JGSS from sulfur-depleted fluids. Furthermore, the elevated Zn concentrations observed in JGSS-2, compared to JGSS-1 and -3, also indicate that Zn is likely leached from sphalerite replaced by fluids and subsequently incorporated into JGSS-2 (Table 1).

The genetic model of JGSS was established based on its crystal structure and chemical composition. The formation of JGSS involves three distinct stages (Fig. 11). In stage 1, Sb- and As-rich fluids interact with galena, leading to the formation of JGSS-1 (As-bearing geocronite, Sb-rich jordanite) along fractures in galena, and JGSS-2 (Sb-rich jordanite, Sb-bearing jordanite) along the margins of galena. During stage 2, with evolving fluids and ongoing replacement of galena, Sb becomes progressively depleted in the fluids, resulting in the formation of abundant JGSS minerals. In stage 3, nearly complete replacement of galena leads to its disappearance and the formation of JGSS-3 (Sb-bearing jordanite) (Fig. 11).

Implication for Fluid Evolution

Jordanite and geocronite are typical in mineral assemblages at the late stage of Pb-Zn mineralization (Fig. 5). The coexistence of these minerals demonstrates that the fluids in the late stage are dominated by Sb and As. The progressive decrease in Sb/As ratios from early JGSS-1 to late JGSS-3 indicates Sb is progressively depleted, whereas As is relatively stable during fluid evolution (Fig. 7). The widespread distribution of JGSS in different locations of an ore body suggests that these minerals may have precipitated nearly simultaneously through the

replacement of galena by Sb- and As-rich fluids under relatively high f_{O_2} and high f_{S_2} conditions (Apopei et al. 2016; Biagioni et al. 2016; Tolstykh et al. 2025).

Sulfosalts are commonly present in the late stage of ore-forming systems. Jordanite, geocronite, JGSS, boulangerite, and tennantite are found in the Bleikvassli Zn-Pb-Cu deposit in Norway, the Coranda-Hondol Pb-Zn deposit in Romania, the Berezitovoe Au deposit in Russia, and the Lizhiping and Fulongchang Pb-Zn-Ag deposits in China (Cook et al. 1998; Apopei et al. 2016; Vakh et al. 2019; Liu et al. 2023). These minerals represent late-stage products of a hydrothermal ore-forming system and can be displayed in geochemical analyses. Birnie and Petersen (1977) were the first to investigate the distribution pattern of As/Sb ratios in JGSS at different locations of Pb-Zn ore bodies in the Huachocolpa mining district, Peru. Their research revealed a well-defined zonation pattern, characterized by a progressive decrease in As/Sb ratios from proximal zones outward from the ore centers. Apopei et al. (2016) demonstrated that the As/Sb ratio in JGSS from the Coranda-Hondol hydrothermal deposit in Romania serves as a robust geochemical proxy for reconstructing hydrothermal fluid flow pathways. In the Huize Pb-Zn deposit, integrated geochemical profiling of JGSS across vertical profiles reveals a systematic decrease in As/(As+Sb) ratios with increasing elevation (Fig. 7b). The observed vertical zonation pattern provides compelling evidence for upward migration of hydrothermal fluids. Moreover, geochemical anomalies of As and Sb or the occurrence of Sb-As-bearing minerals at the surface can be used as reliable indicators for prospecting deep concealed hydrothermal Pb-Zn systems. For example, Li et al. (2018) showed that As and Sb anomalies were mainly distributed in the upper part of the ore body in the Huize deposit and successfully predicted the deep blind ore body by combining with structure and alteration. Therefore, the compositional variations of JGSS in the deposit can be used as a potential exploration indicator for a hydrothermal deposit.

Implications

Sulfosalts in the SYG metallogenic province remain understudied despite their significant scientific and economic potential. This study presents the systematic mineralogical investigations of the newly identified jordanite-geocronite solid solution (JGSS) series in the Huize Pb-Zn deposit. The occurrence of JGSS indicates significant Sb- and As enrichment in the late-stage ore-forming fluids. The formation of JGSS involves multiple fluid-mineral interactions, which are primarily controlled by temperature, f_{O_2}, and f_{S_2}. From the perspective of the variation law of atomic site occupation in the crystal structure of JGSS, the occupation variation trends of As and Sb at different sites provide microscopic evidence for understanding the migration and distribution mechanisms of elements during the mineralization process.

Surface anomalies of As and Sb, along with the presence of Sb-As-bearing sulfosalts, serve as reliable indicators of concealed mineralization at depth. The compositional variations of late-stage sulfosalts, particularly JGSS, offer valuable insights for mineral exploration in hydrothermal systems. Studies from various deposits such as Huize (China), Coranda-Hondol (Romania), and Huachocolpa (Peru) have demonstrated that As/Sb or As/(As+Sb) ratios in JGSS exhibit systematic spatial patterns, typically decreasing from the core of ore bodies outward or from depth to surface. These zonation trends reflect the upward migration of hydrothermal fluids and can be used to trace fluid pathways and vectors toward ore zones. These findings highlight the importance of sulfosalts in understanding ore genesis and assisting mineral exploration.

Acknowledgments and Funding

We thank Shaohua Dong and Wenqin Zheng of the Institute of Geochemistry, Chinese Academy of Sciences, for their guidance on FE-SEM and EPMA. Meanwhile, thanks are given to Di Zhang of the Institute of Geology and Geophysics, Chinese Academy of Sciences, for her help on CAMECA EPMA. We also thank Paul Tomascak, Denis Fougerouse, and three anonymous reviewers for their constructive comments on this manuscript. This research was financially supported by the National Natural Science Foundation of China (92462306, U23A2027, 42473080, 42073043), Provincial Science and Technology Plan Project of Guizhou Province (Qiankehe Foundation-ZK[2023]Key 050), National Key Research and Development Program of China (2021YFC2900300), the Geological Exploration Fund of Guizhou Province (No. 2024-2), CAS "Light of West China" Program to YMM, CAS Hundred Talents Program to XWH, Special Fund of the State Key Laboratory of Ore Deposit Geochemistry (202101 and 202301).

References Cited

Apopei, A.I., Damian, G., Buzgar, N., and Buzatu, A. (2016) Mineralogy and geochemistry of Pb–Sb/As-sulfosalts from Coranda-Hondol ore deposit (Romania)—Conditions of telluride deposition. Ore Geology Reviews, 72, 857–873, https://doi.org/10.1016/j.oregeorev.2015.09.014.

Bao, Z.W., Li, Q., and Wang, C.Y. (2017) Metal source of giant Huize Zn-Pb deposit in SW China: New constraints from in situ Pb isotopic compositions of galena. Ore Geology Reviews, 91, 824–836, https://doi.org/10.1016/j.oregeorev.2017.08.019.

Biagioni, C., Dini, A., Orlandi, P., Moëlo, Y., Pasero, M., and Zaccarini, F. (2016) Lead-antimony sulfosalts from Tuscany (Italy). XX. Members of the jordanite-geocronite series from the Pollone Mine, Valdicastello Carducci: Occurrence and crystal structures. Minerals, 6, 15, https://doi.org/10.3390/min6010015.

Birnie, R.W. and Burnham, C.W. (1976) The crystal structure and extent of solid solution of geocronite. American Mineralogist, 61, 963–970.

Birnie, R.W. and Petersen, U. (1977) The paragenetic association and compositional zoning of lead sulfosalts at Huachocolpa, Peru. Economic Geology and the Bulletin of the Society of Economic Geologists, 72, 983–992, https://doi.org/10.2113/gsecongeo.72.6.983.

Brown, I.D. (1981) The bond-valence method: An empirical approach to chemical structure and bonding. In M. O'Keeffe and A. Navrotsky, Eds., Industrial Chemistry Library, Volume 2, p. 1–30. Elsevier.

Bryzgalov, I.A., Krivitskaya, N.N., and Spiridonov, E.M. (2011) First find of the minerals of jordanite-geocronite-schulzite in one deposit (Darasun, Eastern Transbaikalia). Doklady Earth Sciences, 438, 815–818, https://doi.org/10.1134/S1028334X11060158.

Cook, N.J., Spry, P.G., and Vokes, F.M. (1998) Mineralogy and textural relationships among sulphosalts and related minerals in the Bleikvassli Zn-Pb-(Cu) deposit, Nordland, Norway. Mineralium Deposita, 34, 35–56, https://doi.org/10.1007/s001260050184.

Cui, G.S., Bao, Z.W., Li, Q., and Xiao, Y. (2024) Origin of hydrothermal dolomitization in the Huize Zn-Pb ore district, SW China: Insights from in situ U-Pb dating, fluid inclusion, and C-O-Sr-Mg isotope analyses. Ore Geology Reviews, 173, 106250, https://doi.org/10.1016/j.oregeorev.2024.106250.

Dincă, G., Popescu, G.C., and Topa, D. (2025) Decoding the mineralogy and geochemistry of sulfosalts in the Sacaramb Au-Ag-Te ore deposit (Romania): Unveiling a fresh insight into the evolution of a complex hydrothermal system. Ore Geology Reviews, 176, 106424, https://doi.org/10.1016/j.oregeorev.2024.106424.

Dolomanov, O.V., Bourhis, L.J., Gildea, R.J., Howard, J.A.K., and Puschmann, H. (2009) A complete structure solution, refinement and analysis program. Journal of Applied Crystallography, 42, 339–341, https://doi.org/10.1107/S0021889808042726.

Han, R.S., Liu, C.Q., Huang, Z.L., Li, Y., and Chen, J. (2000) Characteristics of ore-controlling structures and REE composition of fault rocks in Huize lead zinc deposit, Yunnan. Mineralogy and Petrology, 20, 11–18 (in Chinese with English abstract).

Han, R.S., Liu, C.Q., Huang, Z.L., Chen, J., Ma, D.Y., Lei, L., and Ma, G.S. (2007) Geological features and origin of the Huize carbonate-hosted Zn-Pb-(Ag) district, Yunnan, South China. Ore Geology Reviews, 31, 360–383, https://doi.org/10.1016/j.oregeorev.2006.03.003.

Han, R.S., Hu, Y.Z., Wang, X.K., Huang, Z.L., Chen, J., Wang, F., Wu, P., Li, B., Wang, H.J., Dong, Y., and others. (2012) Mineralization model of rich Ge-Ag-bearing Zn-Pb polymetallic deposit concentrated district in northeastern Yunnan, China. Acta Geologica Sinica, 86, 280–294 (in Chinese with English abstract).

Han, R.S., Zhang, Y., Qiu, W.L., Ding, T.Z., Wang, M.Z., and Feng, W. (2023) Geology and geochemistry of Zn-Pb (-Ge-Ag) deposits in the Sichuan-Yunnan-Guizhou Triangle area, China: A review and a new type. Frontiers in Earth Science, 11, 1136397, https://doi.org/10.3389/feart.2023.1136397.

Hu, R.Z. and Zhou, M.F. (2012) Multiple Mesozoic mineralization events in South China—An introduction to the thematic issue. Mineralium Deposita, 47, 579–588, https://doi.org/10.1007/s00126-012-0431-6.

Hu, R.Z., Fu, S.L., Huang, Y., Zhou, M.F., Fu, S.H., Zhao, C.H., Wang, Y.L., Bi, X.W., and Xiao, J.F. (2017) The giant South China Mesozoic low-temperature metallogenic domain: Reviews and a new geodynamic model. Journal of Asian Earth Sciences, 137, 9–34, https://doi.org/10.1016/j.jseaes.2016.10.016.

Huang, Z.L., Li, W.B., Chen, J., Han, R.S., Liu, C.Q., Xu, C., and Guan, T. (2003) Carbon and oxygen isotope constraints on mantle fluid involvement in the mineralization of the Huize super-large Pb-Zn deposits, Yunnan Province, China. Journal of Geochemical Exploration, 78–79, 637–642, https://doi.org/10.1016/S0375-6742(03)00149-3.

Ito, T. and Nowacki, W. (1974) The crystal structure of jordanite, $Pb_{28}As_{12}S_{46}$. Zeitschrift für Kristallographie. Crystalline Materials, 139, 161–185.

Jambor, J.L. (1968) New lead sulfantimonides from Madoc, Ontario; Part 3, Syntheses, paragenesis, origin. Canadian Mineralogist, 9, 505–521.

Karup-Moeller, S. (1971) On some exsolved minerals in galena. Canadian Mineralogist, 10, 871–876.

Krivovichev, V.S. (2013) Structural complexity of minerals: Information storage and processing in the mineral world. Mineralogical Magazine, 77, 275–326, https://doi.org/10.1180/minmag.2013.077.3.05.

Li, C.Y., Liu, Y.P., Zhang, Q., Pi, D.H., Zhang, W.L., and Chen, J. (2005) Discovery of antimony and distribution characteristics of associated elements in Huize Pb-Zn deposit. Mineralium Deposita, 24, 52–60 (in Chinese with English abstract).

Li, W.B., Huang, Z.L., and Yin, M.D. (2007a) Isotope geochemistry of the Huize Zn-Pb ore field, Yunnan Province, Southwestern China: Implication for the sources of ore fluid and metals. Geochemical Journal, 41, 65–81, https://doi.org/10.2343/geochemj.41.65.

——— (2007b) Dating of the giant Huize Zn-Pb ore field of Yunnan Province, Southwest China: Constraints from the Sm-Nd system in hydrothermal calcite. Resource Geology, 57, 90–97, https://doi.org/10.1111/j.1751-3928.2006.00007.x.

Li, X.H., Li, W.X., Li, Z.X., Lo, C.H., Wang, J., Ye, M.F., and Yang, Y.H. (2009) Amalgamation between the Yangtze and Cathaysia Blocks in South China: Constraints from SHRIMP U-Pb zircon ages, geochemistry and Nd-Hf isotopes of the Shuangxiwu volcanic rocks. Precambrian Research, 174, 117–128, https://doi.org/10.1016/j.precamres.2009.07.004.

Li, Z.P., Yu, Z.Z., Luo, D.F., Li, Y.C., W, J., and Li, H. (2018) characteristics of structural superimposed halos and exploration significance of the Qilinchang Pb-Zn deposit, Huize, Yunnan. Geological Science and Technology Information, 37, 109–177 (in Chinese with English abstract).

Li, Z.L., Ye, L., Hu, Y.S., Wei, C., Huang, Z.L., Yang, Y.L., and Danyushevsky, L.V. (2020) Trace elements in sulfides from the Maozu Pb-Zn deposit, Yunnan Province, China: Implications for trace-element incorporation mechanisms and ore genesis. American Mineralogist, 105, 1734–1751, https://doi.org/10.2138/am-2020-6950.

Liu, H.C. and Lin, W.D. (1999) Study on the Pb-Zn-Ag ore deposit in Northeast Yunnan, China, p. 1–468. Yunnan University Press (in Chinese).

Liu, Y.F., Qi, H.W., and Lin, W.J. (2023) Study on mineral chemistry of Liziping-Fulongchang Pb-Zn-Ag deposit in Western Yunnan and its metallogenic significance. Journal of South China Normal University, 55, 17–28 (Natural Science Edition).

Luo, K., Zhou, J.X., Huang, Z.L., Caulfield, J., Zhao, J.X., Feng, Y.X., and Ouyang, H.G. (2020) New insights into the evolution of Mississippi Valley-Type hydrothermal system: A case study of the Wusihe Pb-Zn deposit, South China, using quartz in-situ trace elements and sulfides in situ S-Pb isotopes. American Mineralogist, 105, 35–51, https://doi.org/10.2138/am-2020-7021.

Meng, Y.M., Hu, R.Z., Huang, X.W., Gao, J.F., and Sasseville, C. (2019) The origin of the carbonate-hosted Huize Zn–Pb–Ag deposit, Yunnan province, SW China: Constraints from the trace element and sulfur isotopic compositions of pyrite. Mineralogy and Petrology, 113, 369–391, https://doi.org/10.1007/s00710-019-00654-2.

Meng, Y.M., Zhang, X., Huang, X.W., Hu, R.Z., Bi, X.W., Meng, S.N., Zhou, L.L., and Zheng, Y. (2024) A review of the Zn-Pb deposits in Sichuan-Yunnan-Guizhou metallogenic region with emphasis on the enrichment mechanism of Ge, Ga and In. Ore Geology Reviews, 164, 105853, https://doi.org/10.1016/j.oregeorev.2023.105853.

Metcalfe, I. (2013) Gondwana dispersion and Asian accretion: Tectonic and palaeogeographic evolution of eastern Tethys. Journal of Asian Earth Sciences, 66, 1–33, https://doi.org/10.1016/j.jseaes.2012.12.020.

Mi, M., Chen, Y.J., Yang, Y.F., Wang, P., Li, F.L., Wan, S.Q., and Xu, Y.L. (2015) Geochronology and geochemistry of the giant Qian'echong Mo deposit, Dabie Shan, eastern China: Implications for ore genesis and tectonic setting. Gondwana Research, 27, 1217–1235, https://doi.org/10.1016/j.gr.2014.05.006.

Moëlo, Y. (1983) Contribution à l'étude des conditions naturelles de formation des sulfures complexes d'antimoine et plomb (Sulfosels de Pb/Sb): Signification métallogénique. Orléans: Bureau de recherches g'éologiques et miniéres, 85–116.

Moëlo, Y., Makovicky, E., Mozgova, N.N., Jambor, J.L., Cook, N., Pring, A., Paar, W., Nickel, E.H., Graeser, S., Karup-Moller, S., and others. (2008) Sulfosalt systematics: A review. Report of the sulfosalt sub-committee of the IMA Commission on Ore Mineralogy. European Journal of Mineralogy, 20, 7–46, https://doi.org/10.1127/0935-1221/2008/0020-1778.

Niu, P.P., Muñoz, M., Mathon, O., Xiong, S.F., and Jiang, S.Y. (2024) Mechanism of germanium enrichment in the world-class Huize MVT Pb-Zn deposit, southwestern China. Mineralium Deposita, 59, 995–1016, https://doi.org/10.1007/s00126-023-01242-3.

Oyebamiji, A., Falae, P., Zafar, T., Rehman, H.U., and Oguntuase, M. (2023) Genesis of the Qilinchang Pb-Zn deposit, southwestern China: Evidence from mineralogy, trace elements systematics and S-Pb isotopic characteristics of sphalerite. Applied Geochemistry, 148, 105545, https://doi.org/10.1016/j.apgeochem.2022.105545.

Qiu, D.M. (2000) The Upper lead-zinc deposit in the Jinsha mining district, Yongshan, Yunnan. Chenji Yu Tetisi Dizhi, 2, 83–91 (in Chinese with English abstract).

Renock, D. and Becker, U. (2011) A first principles study of coupled substitution in galena. Ore Geology Reviews, 42, 71–83, https://doi.org/10.1016/j.oregeorev.2011.04.001.

Roland, G.W. (1968) The system Pb-As-S. Mineralium Deposita, 3, 249–260, https://doi.org/10.1007/BF00207438.

Shannon, R.D. (1976) Revised effective ionic radii and systematic studies of interatomic distances in halides and chalcogenides. Acta Crystallographica Section A, 32, 751–767, https://doi.org/10.1107/S0567739476001551.

Sheldrick, G.M. (2015) Crystal structure refinement with SHELXL. Acta Crystallographica Section C, 71, 3–8, https://doi.org/10.1107/S2053229614024218.

Shu, Z.X., Li, S., and Gu, X.P. (2018) First discovery of jordanite in China and its mineralogical features. Acta Petrologica et Mineralogica, 37, 853–859 (in Chinese with English abstract).

Slater, E.T., McDonald, A.M., and Kontak, D.J. (2019) Resolving primary and retrograde sulfide and sulfosalt textures in the epithermal Ag-Zn-Pb-Sn-rich Cortaderas Zone, Pirquitas Mine, Argentina. Canadian Mineralogist, 57, 117–143, https://doi.org/10.3749/canmin.1700076.

Sun, C., Zhang, H.S., Yang, X.Y., Ji, W.H., Chen, B., Li, Y.G., Dong, Z.C., Faisal, M., Jin, M.Q., and Zhao, X.J. (2023) A tale of elemental accumulation and recycling in the metamorphosed Keketale VMS-type Pb-Zn deposit, Altai Mountains. Geoscience Frontiers, 14, 101481, https://doi.org/10.1016/j.gsf.2022.101481 (in Chinese with English abstract).

Svanberg, L.F. (1840) Untersuchung des geokronit und hydrophit, zweier in Schweden vorkommenden neuen mineralien. Annalen der Physik, 127, 535–538, https://doi.org/10.1002/andp.18401271210.

Tan, M., Huang, X.W., Wu, P., and Huang, Z.L. (2023) Ore-forming process of the Huize super-large Pb-Zn deposit, SW China: Constraints from in situ elements and S-Pb isotopes. Ore Geology Reviews, 159, 105580, https://doi.org/10.1016/j.oregeorev.2023.105580.

Tang, Y.Y., Bi, X.W., Zhou, J.X., Liang, F., Qi, Y.Q., Leng, C.B., Zhang, X.C., and Zhang, H. (2019) Rb-Sr isotopic age, S-Pb-Sr isotopic compositions and genesis of the ca. 200 Ma Yunluheba Pb-Zn deposit in NW Guizhou Province, SW China. Journal of Asian Earth Sciences, 185, 104054, https://doi.org/10.1016/j.jseaes.2019.104054.

Tolstykh, N.D., Shapovalova, M.O., and Chubarov, V.M. (2025) Evolution of composition of tetrahedrite and enargite sulfosalts in the Maletoyvayam epithermal Au-Ag deposit (Kamchatka). Russian Geology and Geophysics, 66, 613–629, https://doi.org/10.2113/RGG20244818.

Vakh, A.S., Avchenko, O.V., Goryachev, N.A., Gvozdev, V.I., and Karabtsov, A.A. (2016) New data on the composition of jordanite-geocronite Pb–Sb–As sulfosalts at the Berezitovoe deposit (Upper Amur Region, Russia). Doklady Earth Sciences, 467, 402–407, https://doi.org/10.1134/S1028334X16040231.

Vakh, A.S., Avchenko, O.V., Gvozdev, V.I., Goryachev, N.A., Karabtsov, A.A., and Vakh, E.A. (2019) Minerals of the Pb-As-Sb-S and Cu-Pb-As-Sb-S systems in ores of the Berezitovoe Gold-Polymetallic deposit, Upper Amur Region, Russia. Geology of Ore Deposits, 61, 256–273, https://doi.org/10.1134/S1075701519020065.

Walia, D.S. and Chang, L.L.Y. (1973) Investigations in the systems PbS-Sb_2S_3-As_2S_3 and PbS-Bi_2S_3-As_2S_3. Canadian Mineralogist, 12, 113–119.

Wang, X.C., Li, Z.X., Li, X.H., Li, Q.L., Tang, G.Q., Zhang, Q.R., and Liu, Y. (2011) Nonglacial origin for low-$\delta^{18}O$ Neoproterozoic magmas in the South China Block: Evidence from new in-situ oxygen isotope analyses using SIMS. Geology, 39, 735–738, https://doi.org/10.1130/G31991.1.

Wang, Q.F., Deng, J., Li, C.S., Li, G.J., Yu, L., and Qiao, L. (2014) The boundary between the Simao and Yangtze blocks and their locations in Gondwana and

Rodinia: Constraints from detrital and inherited zircons. Gondwana Research, 26, 438–448, https://doi.org/10.1016/j.gr.2013.10.002.
Wu, T., Zhou, J.X., Wang, X.C., Li, W.X., Wilde, S.A., Sun, H.R., Wang, J.S., and Li, Z. (2018) Identification of ca. 850 Ma high-temperature strongly peraluminous granitoids in southeastern Guizhou Province, South China: A result of early extension along the southern margin of the Yangtze Block. Precambrian Research, 308, 18–34, https://doi.org/10.1016/j.precamres.2018.02.007.
Yan, D.P., Zhou, M.F., Song, H.L., Wang, X.W., and Malpas, J. (2003) Origin and tectonic significance of a Mesozoic multi-layer over-thrust system within the Yangtze Block (South China). Tectonophysics, 361, 239–254, https://doi.org/10.1016/S0040-1951(02)00646-7.
Yao, Y.S., Gong, H.S., Han, R.S., Zhang, C.Q., Wu, P., and Chen, G. (2023) Metallogenesis and formation of the Maliping Pb-Zn deposit in Northeastern Yunnan: Constraints from H-O isotopes, fluid inclusions, and trace elements. Minerals, 13, 780, https://doi.org/10.3390/min13060780.
Zhang, C.Q., Mao, J.W., Liu, F., and Li, H.M. (2005) K-Ar dating of altered clay minerals from Huize Pb-Zn deposit in Yunnan Province and its geological significance. Mineralium Deposita, 24, 317–324 (in Chinese with English abstract).
Zhang, C.Q., Wu, Y., Hou, L., and Mao, J.W. (2015) Geodynamic setting of mineralization of Mississippi Valley-type deposits in world-class Sichuan-Yunnan-Guizhou Zn-Pb triangle, southwest China: Implications from age-dating studies in the past decade and the Sm-Nd age of Jinshachang deposit. Journal of Asian Earth Sciences, 103, 103–114, https://doi.org/10.1016/j.jseaes.2014.08.013.
Zhang, H., Zhou, J.X., Zhou, M.F., Yue, Z.P., and He, Y. (2024) Zinc isotopes revealed the role of ore-hosting carbonate rocks in the formation of MVT deposits: A case study of the Huize Pb-Zn deposit, SW China. Journal of Geochemical Exploration, 258, 107396, https://doi.org/10.1016/j.gexplo.2024.107396.
Zhao, J.H., Zhou, M.F., Yan, D.P., Zheng, J.P., and Li, J.W. (2011) Reappraisal of the ages of Neoproterozoic strata in South China: No connection with the Grenvillian orogeny. Geology, 39, 299–302, https://doi.org/10.1130/G31701.1.
Zhao, W.C., Jiang, B.B., Zhu, X.Y., Guan, Y.C., and Zhao, D.S. (2023) Structural and geochemical constraints on the genesis of the Kuangshanchang carbonate-hosted zinc-lead deposit, Huize district, southwestern Yangtze Craton. International Journal of Earth Sciences, 112, 1251–1275, https://doi.org/10.1007/s00531-023-02303-8.
Zhou, C.X., Wei, C.S., Guo, J.Y., and Li, C.Y. (2001) The source of metals in the Qilinchang Zn-Pb deposit, northeastern Yunnan, China: Pb-Sr isotope constraints. Economic Geology and the Bulletin of the Society of Economic Geologists, 96, 583–598, https://doi.org/10.2113/gsecongeo.96.3.583.
Zhou, M.F., Yan, D.P., Kennedy, A.K., Li, Y.Q., and Ding, J. (2002) SHRIMP U-Pb zircon geochronological and geochemical evidence for Neoproterozoic arc-magmatism along the western margin of the Yangtze Block, South China. Earth and Planetary Science Letters, 196, 51–67, https://doi.org/10.1016/S0012-821X(01)00595-7.
Zhou, J.X., Huang, Z.L., and Bao, G.P. (2013) Geological and sulfur–lead–strontium isotopic studies of the Shaojiwan Pb–Zn deposit, southwest China: Implications for the origin of hydrothermal fluids. Journal of Geochemical Exploration, 128, 51–61, https://doi.org/10.1016/j.gexplo.2013.01.007.

Manuscript received December 2, 2024
Manuscript accepted August 1, 2025
Accepted manuscript online August 13, 2025
Manuscript Handled by Denis Fougerouse

Endnotes:

[1]Deposit item AM-26-39708. Online Materials are free to all readers. Go online, via the table of contents or article view, and find the tab or link for supplemental materials.